

Galaxy Secular Mass Flow Rate Determination Using the Potential-Density Phase Shift Approach: Application to Six Nearby Spiral Galaxies

Xiaolei Zhang

Department of Physics and Astronomy, George Mason University, 4400 University Drive, Fairfax, VA 22030, USA
E-mail: xzhang5@gmu.edu

Ronald J. Buta

Department of Physics and Astronomy, University of Alabama, 514 University Blvd E, Box 870324, Tuscaloosa, AL 35487, USA
E-mail: buta@sarah.astr.ua.edu

Abstract

Using the potential-density phase shift approach developed by the present authors in earlier publications, we estimate the magnitude of radial mass accretion/excretion rates across the disks of six nearby spiral galaxies (NGC 628, NGC 3351, NGC 3627, NGC 4321, NGC 4736, and NGC 5194) having a range of Hubble types. Our goal is to examine these rates in the context of bulge building and secular morphological evolution along the Hubble sequence. Stellar surface density maps of the sample galaxies are derived from SINGS $3.6\mu\text{m}$ and SDSS i -band images using colors as an indicator of mass-to-light ratios. Corresponding molecular and atomic gas surface densities are derived from published CO(1-0) and HI interferometric observations of the BIMA SONG, THINGS, and VIVA surveys. The mass flow rate calculations utilize a volume-type torque integral to calculate the angular momentum exchange rate between the basic state disk matter and what we assume to be density wave *modes* in the observed galaxies. This volume-type integral contains the contributions from both the gravitational surface torque couple and the advective surface torque couple at the nonlinear, quasi-steady state of the wave modes, in sharp contrast to its behavior in the linear regime, where it contains only the contribution from the gravitational surface torque couple used by Lynden-Bell & Kalnajs in 1972. The potential-density phase shift approach yields angular momentum transport rates several times higher than those estimated using the Lynden-Bell and Kalnajs approach. And unlike Lynden-Bell and Kalnajs, whose approach predicts zero mass redistribution across the majority of the disk surface (apart from the isolated locations of wave-particle resonances) for quasi-steady waves, the current approach leads to predictions of significant mass redistribution induced by the quasi-steady density wave modes, enough for the morphological types of disks to evolve substantially within its lifetime. This difference with the earlier conclusions of Lynden-Bell and Kalnajs reflects the dominant role played by collisionless shocks in the secular evolution of galaxies containing extremely non-linear, quasi-steady density wave modes, thus enabling significant morphological transformation along the Hubble sequence during a Hubble time. We show for the first time also, using observational data, that *stellar* mass accretion/excretion is just as important, and oftentimes much more important, than the corresponding accretion/excretion processes in the *gaseous* component, with the latter being what had been emphasized in most of the previous secular evolution studies.

Keywords: galaxies: kinematics and dynamics; galaxies: structure; galaxies: evolution; galaxies: spiral

1. INTRODUCTION

The potential-density phase shift (PDPS), referring to a characteristic radial distribution of the azimuthal offset between the gravitational potential minimum and the density maximum of a skewed internal gravitational perturbation (such as a skewed bar or an open spiral), has been shown to be both the driver as well as the result of

a collective dissipation process occurring in any gravitational N -body disks having self-organized, quasi-steady nonlinear density wave *modes*, (Zhang 1996, 1998, 1999. Hereafter Z96, Z98, Z99). The PDPS can be determined from observations of galaxies, and its magnitude and distribution shed important light on the secular evolution of the stellar and gaseous distributions in disk

galaxies of different Hubble types.

Zhang & Buta (2007=ZB07) made the first demonstration that the PDPS approach can be used on observed galaxy images to determine two quantities of dynamical interest, for those galaxies containing self-organized density wave modes: the locations of the *corotation resonance (CR) radii* of individual modes, and the rate of radial mass accretion/excretion as a function of radius as a result of the interaction between these modes and the basic state of the galactic disks. Subsequently, Buta & Zhang (2009=BZ09) applied the PDPS approach to locate the CR radii in 153 galaxies using near-infrared *H*-band images from the Ohio State University Bright Spiral Galaxy Survey (OSUBSGS, Eskridge et al. 2002), and brought attention to a range of characteristic bar-spiral combinations, as well as their associated characteristic PDPS distributions, among normal galaxies (some examples of these characteristic bar-spiral combinations will be further discussed in Appendix B of the current paper in the context of secular morphological evolution of galaxies). Among the original findings of ZB07 and BZ09 is the so-called “super-fast” bar, where the bar corotation radius lies inside the ends of the bar, in contradiction to the previous conclusion of Contopoulos (1980), obtained using passive orbit analysis ignoring the collective interactions of stars in a self-organized bar *mode*, that a bar cannot extend beyond its own CR. This finding alone shows that the PDPS approach can lead to new insights into galaxy dynamical states that had not been considered previously.

In this paper, our focus is on observational estimates of mass flow rates in a small sample of galaxies over a range of Hubble types. Our goals are two-fold: to outline how to use the PDPS method to estimate galaxy mass flow rates, and to examine the implications of these rates with regard to angular momentum transport, bulge-building, and long-term secular morphological evolution of galaxies.

1.1. Application of the PDPS Approach

Observationally, measuring phase shift distributions, mass flow rates, and torque couplings in galaxies using the PDPS approach requires mainly a two-dimensional map of the surface mass density distribution, $\Sigma(x, y)$, in units of $M_{\odot}pc^{-2}$. Reasonable approximations to *stellar* surface mass densities can be inferred from calibrated images using mass-to-light ratio estimates, which are often based on the colors of the light. The preferred passbands for this kind of calculation have been the near- and mid-infrared, where the starlight more reliably traces the mass of the old stellar population, and where

extinction effects are much lower than in optical bands (Meidt et al. 2012). An important assumption is that we can reasonably deproject galaxy images by assuming outer isophotes are intrinsically circular. To minimize deprojection uncertainties, we limit our analysis in the current study only to relatively face-on galaxies. In contrast to the analysis in ZB07 and BZ09, which considered only the stellar mass surface densities, in the current work we include also the contributions from atomic and molecular gas, obtained from archival radio interferometric observations, to the determination of the total surface mass density of the galaxy disks.

In calculating the two-dimensional gravitational potential $\mathcal{V}(x, y)$ used in the PDPS approach, we applied the standard Poisson integral approach to the total surface density map $\Sigma(x, y)$, employing the fast Fourier transform technique similar to that used in Quillen et al. (1994). We have experimented with various forms of the vertical density distribution in ZB07 and BZ09, and found that these different choices of profiles (including exponential, sech, or sech-squared functions) led to moderate differences in the magnitude of the potential obtained, but negligible difference in the locations of resonances determined through the PDPS approach.

Our main *working hypothesis* is that the features we see in disk galaxies are *quasi-stationary wave modes*, meaning they are long-lived. This is at the moment still not a universally accepted assumption. For example, Sellwood (2011) argues that short-lived transient patterns are the rule in simulations. On the other hand, detection of azimuthal color-age gradients across spiral arms, predicted by density wave theory, favors that the patterns are long-lived (González & Graham 1996; Martínez-García et al. 2009a,b; Martínez-García & González-Lópezlira 2011). The presence of well-organized nested resonance patterns in grand-design galaxies such as NGC 4321 (one of our sample galaxies) also supports the quasi-steady modal origin of these patterns. The success of the PDPS approach itself in accurately predicting the location of CR radii¹, is also an indirect confirmation of the modal origin of the density wave patterns in grand-design galaxies, because such an agreement should not be expected in the transient wave picture. *Thus we adopt as our working hypothesis that the density wave patterns in grand design disk galaxies are quasi-steady modes, and then examine if*

¹Haan et al. (2009) had independently accessed several CR radii determination methods and stated that “For our galaxies the phase-shift method appears to be the most precise method with uncertainties of (5-10)% ...” (Haan et al. 2009, ApJ, 692, 1623), Their above statement appears in page 1641, left column and second full paragraph.

the consequences derived from this assumption contradict with the observed properties of galaxies. Note that for the dynamical mechanism described in Z96, Z98, Z99 to work in predicting the secular mass flow rate, the modes only need to be quasi-steady on a local dynamical timescale, i.e., a few galactic rotation periods at a characteristic radius of the galaxy, rather than the more stringent stability requirement on a Hubble time, which would be unrealistic to expect given the significant basic state evolution produced by these nonlinear modes. The evolving basic state of the galactic disk will gradually change the modal set and modal morphology compatible with it.

Our application of the PDPS approach will be based on several equations. The first is the radial distribution of the phase shift itself (Z96, Z98), which will be used to locate CR radii in each galaxy:

$$\phi_0(r) = \frac{1}{m} \sin^{-1} \left(\frac{1}{m} \frac{\int_0^{2\pi} \Sigma_1 \frac{\partial \mathcal{V}_1}{\partial \phi} d\phi}{\sqrt{\int_0^{2\pi} \mathcal{V}_1^2 d\phi} \sqrt{\int_0^{2\pi} \Sigma_1^2 d\phi}} \right), \quad (1)$$

where m is the azimuthal order of the perturbation, and ϕ_0 is defined to be positive if the potential lags the density in the azimuthal direction, in the sense of galactic rotation, and negative if it leads the density. For most galaxies the sense of galactic rotation can be determined by the assumption that the density wave pattern is trailing. In the above expression, $\Sigma_1(r, \phi)$ and $\mathcal{V}_1(r, \phi)$ are the nonaxisymmetric parts of the surface mass density and gravitational potential, respectively. From considerations of the angular momentum exchange between the axisymmetric basic state and the spontaneously-formed mode, it can be inferred that the radial phase shift distribution of a single quasi-steady mode has one positive hump followed by one negative hump (Z98), with the zero crossing of the PDPS curve between these two humps occurring at CR. Multiple modes in the same galaxy would be manifested as a sequence of (positive, negative) hump pairs. Each positive-to-negative (P/N) zero crossing of the phase-shift-versus-radius curve would correspond to the CR radius of a single mode – if the underlying modal pattern is indeed in a quasi-steady state. Note that for the purpose of locating CR radii, no knowledge of the distance of the galaxy is required since a constant mass-to-light ratio can lead already to fairly accurate CR determination (ZB07).

The validity of using the P/N zero-crossings of the PDPS distribution for locating CR radii does *not* rely on the spiral/bar modes being exactly steady, only that they are modes (i.e., the approach is equally valid if

the mode is uniformly growing and uniformly decaying, while maintaining the modal shape – this has been seen in many N-body simulations of spiral modes, such as Donner & Thomasson 1994; Z98). The validity of the PDPS approach in determining CRs is reduced if there is spurious non-modal content in the pattern surface density that is in the process of being filtered out by the galactic resonant cavity (i.e., if the mode is in the very early stages of growing out of primordial inhomogeneous clumps, or else is due to tidal excitation). Another issue regarding equation 1 is that P/N crossings are not affected by the assumed value of m .

The second equation we will use is the mass flow rate as a function of radius (Z96, Z98, ZB07, note that the minus sign present in front of the integral sign for this equation in ZB07, which was a typo, is now taken out. The sign convention is for dM/dt to be greater than zero for accretion inside R , and less than zero for excretion)

$$\frac{dM(R)}{dt} = \frac{R}{V_c} \int_0^{2\pi} \Sigma_1 \frac{\partial \mathcal{V}_1}{\partial \phi} d\phi \quad (2)$$

where R is the radius, V_c is the circular velocity, and Σ_1 and \mathcal{V}_1 denote the perturbed surface mass density and potential, respectively. Σ_1 in particular can denote the perturbative surface density of a given mass component (i.e., stars or gas), but \mathcal{V}_1 used needs to be the total potential – this is because the accretion mass cannot separate the forcing field component, and responds only to the *total* forcing potential². In actual calculations, one can in fact employ the sum total of perturbative and non-perturbation mass components, since the axisymmetric parts will naturally drop out through the differentiation and integration process.

Equations 1 and 2 both show that if Σ_1 and \mathcal{V}_1 are exactly in phase with each other, which can result for either an extremely tightly-wound spiral or a perfectly straight bar (Z96,Z98), then there would be no angular momentum exchange between the wave and the disk matter in an annulus and no radial mass flow. For open (skewed) spirals or bars, there will always be a phase shift as a result of the Poisson integral (this in fact is a result of earlier potential theory studies by mathematicians of the 19th century, though no kinematic information was included in such studies and thus no corotation determination was considered). For spontaneously-formed modes, its basic state density distribution will

²Dark matter is not included in our analysis because its skewness is assumed to be small – and if this is not the case, the derived accretion rate will be higher than what we obtained in this study.

be such that the phase shift changes sign at corotation, leading to wave-basic-state angular momentum exchange at the quasi-steady state of the modes and the secular mass redistribution of the basic state, specifically, mass inflow inside CR and mass outflow outside CR. The exact validity of equation 2 for calculating the basic state mass flow rate depends on the quasi-steady state assumption (Z96, Z98, Z99, once again note that “quasi-steady” here refers to modal pattern maintaining its shape on the order of local dynamical time), but even for the non-steady situation, equation 2 can be used to estimate an approximate mass flow rate. In addition to the Σ and \mathcal{V} maps, application of equation 2 requires knowledge of the galaxy rotation curve and the distance.

Other quantities used in the following include gravitational and advective (surface) torque couplings (Lynden-Bell & Kalnajs 1972 = LBK72), in order to examine the secular angular momentum redistribution rate. Employing the notation used by Binney & Tremaine (2008=BT08), the gravitational torque coupling integral $C_g(R)$ can be obtained from

$$C_g(R) = \frac{R}{4\pi G} \int_{-\infty}^{\infty} \int_0^{2\pi} \frac{\partial \mathcal{V}}{\partial \phi} \frac{\partial \mathcal{V}}{\partial R} d\phi dz, \quad (3)$$

and the advective torque coupling integral $C_a(R)$ can be obtained from

$$C_a(R) = R^2 \int_0^{2\pi} \Sigma_0 V_R V_\phi d\phi, \quad (4)$$

where V_R and V_ϕ are the radial and azimuthal velocity perturbations relative to the circular velocity, respectively. The gravitational torque couple is due to the torquing of the inner disk material on the outer disk material, or vice versa, across the relevant surface under consideration, through gravitational interaction; whereas the advective torque couple accounts for the angular momentum exchange between the inner and outer disk carried by the matter crossing the same surface during the different phases of the galactic rotation with respect to the phases of the density wave (i.e. the so-called lorry transport effect, or Reynolds stress, see LKB72 or BT08).

The mass flow rate formula involves a volume-type of torque integral that can be related to the above two surface-type torque couplings. The integral,

$$T_1(R) \equiv R \int_0^{2\pi} \Sigma_1 \frac{\partial \mathcal{V}_1}{\partial \phi} d\phi, \quad (5)$$

was introduced in Z96 and Z98 in the context of the self-torquing of the disk matter in a unit-width annulus at R

by the potential of the associated spontaneously-formed density wave mode (effectively the torque on the matter in the annulus is applied by matter both in the inner disk and in the outer disk away from the annulus). The volume torque can be shown to be equal to the time rate of angular momentum exchange between the density wave and the disk matter in a unit-width annulus at R , for wave modes in approximate quasi-steady state. For such modes, Z99 showed that $T_1(R) = d(C_a + C_g)/dR$, and thus accounts for both types of surface torque couple contributions.

Past calculations of the secular angular momentum redistribution rate [i.e. Gnedin et al. (1995), Foyle et al. (2010)] considered only the gravitational torque couple and ignored the advective torque couple (which cannot be directly estimated using the observational data, except by estimating the total volume torque $T_1(R)$, performing a radial integration, and then subtracting from it the contribution of the gravitational torque). The results in section 2.3 below show that for the typical density wave amplitudes usually encountered in observed galaxies, the advective contribution to the total torque couple is several times larger than the contribution from the gravitational torque, and also is of the same sense of angular momentum transport as the gravitational torque couple – another characteristic unique to the nonlinear mode. Past calculations of gas mass accretion near the central region of galaxies (e.g. Haan et al. 2009) are likely to have significantly underestimated the gas mass flow rate for the same reason.

2. ANALYSES OF INDIVIDUAL GALAXIES

In this section, we begin by analyzing the morphology and kinematics of six bright, nearby galaxies, to set the stage for further evolutionary studies in the latter part of this section. The parameters of these galaxies are given in Table 1. For five of the galaxies, two stellar mass maps were derived, one based on a SINGS (Kennicutt et al. 2003) $3.6\mu\text{m}$ IRAC image, and the other based on a SDSS i -band image. HI and H₂ gas maps from archival radio interferometric observations were then added onto these stellar surface density maps to obtain the total disk surface density maps. The procedure for calculating all maps is described in Appendix A. We note that hot dust corrections had to be made to the $3.6\mu\text{m}$ maps, and that no bulge/disk decompositions in this instance were made to allow for bulge shapes.

The total-mass maps derived are shown in Figure 1. Since parts of the discussions in this section concern CR radii, Appendix B gives schematic representations of

Table 1: Adopted parameters for sample galaxies.^a

Galaxy	i (degrees)	ϕ_n (degrees)	h_R (arcsec)	h_z (arcsec)	Distance (Mpc)	References for (i, ϕ_n)
NGC 628	6	25	64 (3.6)	7.1	8.2	Shostak et al. (1983)
NGC 3351	40.6	13.3	44 (3.6)	8.9	10.1	3.6 μ m isophotes
NGC 3627	60	173	66 (3.6)	13.3	10.1	RC2, Zhang et al. (1993)
NGC 4321	31.7	153	63 (3.6)	12.6	16.1	Hernandez et al. (2005)
NGC 4736	30	116	135 (i)	27.1	5.0	3.6 μ m, g,i isophotes; Buta (1988)
NGC 5194	20 \pm 5	170 \pm 3	50 (K_s)	10.0	7.7	Tully (1974)

^aCol. 1: galaxy name; col. 2: adopted inclination; col. 3: adopted line of nodes position angle; col. 4: adopted radial scale length, not based on decomposition but from slope of azimuthally-averaged surface brightness profile (filter used in parentheses); col. 5: adopted vertical scale height derived as $h_z = h_R/5$ except for NGC 628 where $h_z = h_R/9$; col. 6: mean redshift-independent distance from NED; typical uncertainty ± 1 -2Mpc; col. 7: source of adopted orientation parameters.

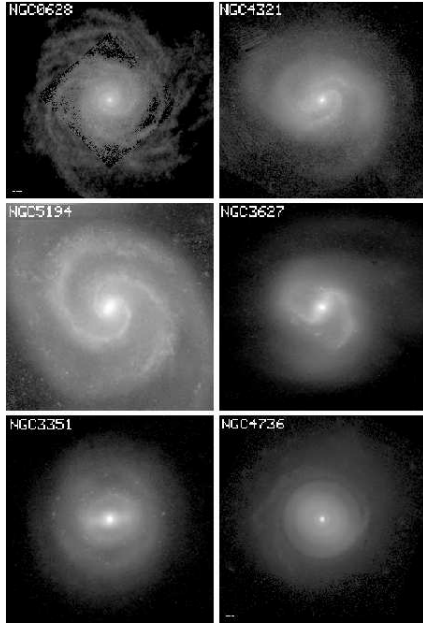


Figure 1: Total mass maps of the six sample galaxies.

the different kinds of bar-spiral configurations described by BZ09, including slow, fast, and super-fast types.

2.1. Phase Shifts and Corotation Resonances

2.1.1. NGC 4321 (M100)

NGC 4321 (M100) is the bright Virgo spiral, of mid-infrared (MIR) RC3 type SAB(rs, nr)bc (Buta et al. 2010). It lies at a distance of approximately 16 Mpc. The surface densities of the gaseous mass components HI and H₂, derived from VIVA (Chung et al. 2009) and

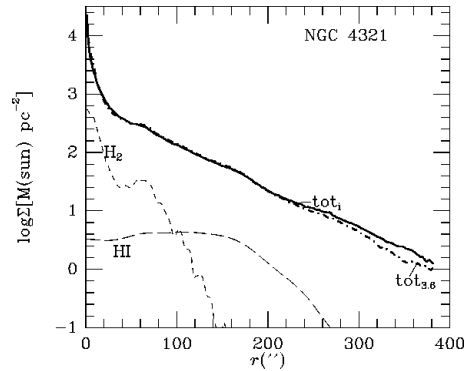


Figure 2: Azimuthally-averaged surface mass density profiles of NGC 4321, based on the atomic (HI), molecular (H₂), and total (3.6 μ m + HI + H₂ and i + HI + H₂) mass maps. The profile based on the 3.6 μ m image is called tot_{3,6} while that based on the i -band is called tot _{i} .

BIMA SONG (Helfer et al. 2003) observations, respectively, and the total mass profiles using the IRAC 3.6 μ m image and the SDSS i -band image (“tot_{3,6}” and “tot _{i} ”, respectively), are illustrated in Figure 2 for this galaxy. This shows that the 3.6 μ m and i -band total mass maps give very similar average surface density distributions for M100.

ZB07 presented a phase shift analysis for M100 using the 3.6 μ m SINGS image, and assumed a constant mass to light ratio (M/L) without gas. (Our current analysis allows for color-dependent stellar M/L corrections.) Four corotation resonances (CRs) were found, and were shown to correspond to well-defined morphological features. Figure 3, top, shows the radial-dependence of potential-density phase shift derived using the *total* (stellar plus gaseous) maps for the IRAC

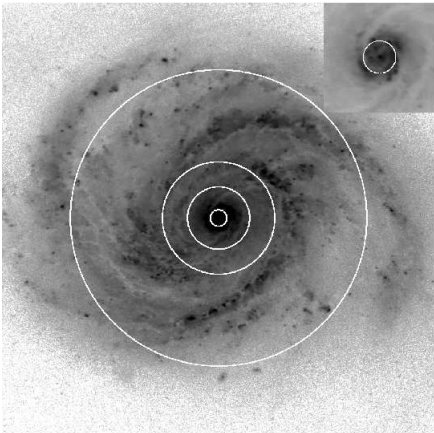
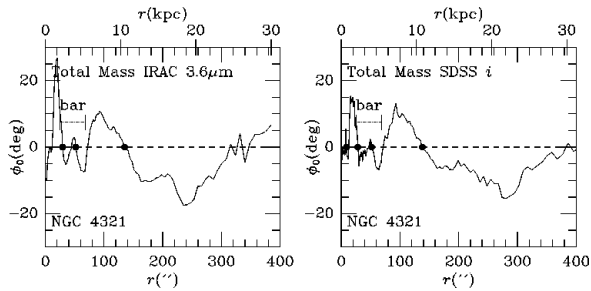


Figure 3: *Top*: Potential-density phase shift versus galactic radius for NGC 4321 derived using the total mass map with IRAC and SDSS data. CR radii are indicated by the filled circles. The radius range of the bar from ZB07 is indicated. *Bottom*: Corotation circles overlaid on a deprojected SDSS g -band image of NGC 4321. The main frame covers an area $6'.4$ square, while the inset is $0'.8$ square. The units are mag arcsec^{-2} .

$3.6 \mu\text{m}$ band (left frame) and the SDSS i -band (right frame). We can see that these two maps give similar CR predictions [in terms of the positive-to-negative (P/N) zero crossings of the phase shift curves], except near the very center of the galaxy where the factor of 2 better spatial resolution of the SDSS map allows the possible detection of a new inner nuclear pattern. We have also conducted tests by calculating phase shift distributions using images from the different optical and NIR wave bands that we have access to, assuming constant M/L, and found that the phase shifts derived from the above total mass maps (calibrated with radial dependent M/L) show the best coherence, most likely due to the best kinematical and dynamical mutual consistency between the potential and density pair used for the total mass analysis, as is the case for physical galaxies. Table 2 lists the (unweighted) average CR radii from the $3.6\mu\text{m}$ and i -band maps.

Figure 3, bottom shows the four CR circles for M100 superposed on the g -band SDSS image. The inset shows only the inner region, which in the g -band includes a nuclear pseudoring and in the longer wavelength bands includes a nuclear bar. The CR₁ radius determined from the new maps, ($8''.3 \pm 0''.7$) is smaller than what we obtained previously ($13''$) in ZB07, but turns out to better correspond to the features of the resolved inner bar. The nuclear bar seems to extend either a little beyond or just up to its CR and terminates in a broad, swept-up spiral section (a nuclear pseudoring) at the location indicated by the next N/P crossing. The next CR, CR₂, appears to be related to an inner spiral that breaks from near the nuclear pseudoring. The curved dust lanes in this spiral are on the leading sides of the weak bar. CR₃ appears to lie completely within the main spiral arms and could be the CR of the bar itself. The radius of CR₃, $52''$, is slightly less than that determined by ZB07, $59''$, and may lie a little inside the ends of the primary bar. CR₄, at $137''$, lies within the outer arms. These values should be compared with $r(\text{CR}) = 97'' \pm 15''$ obtained by Hernandez et al. (2005) using the Tremaine-Weinberg method applied to an $\text{H}\alpha$ velocity field. Their value is close to the average of our CR₃ and CR₄ radii. We believe our two-outer-CR result is more reasonable than the single outer CR result from the TW method for this galaxy, because on the g -band overlay image one can clearly discern the dust lanes moving from the inner/leading edge of the spiral to outer/trailing edge across CR₄, indicating the location where the angular speeds of disk matter and density wave switch their relative magnitude. CR₃ on the other hand is tied to the main bar rather than the spiral.

It appears that the patterns surrounding CR₁ and CR₃

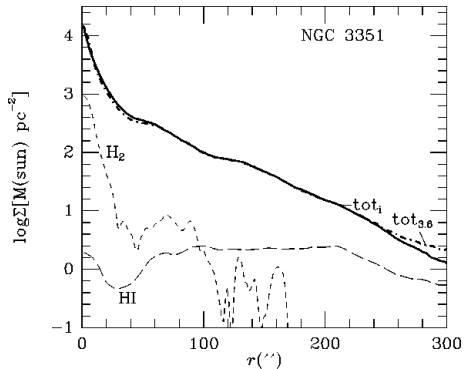


Figure 4: Azimuthally-averaged surface mass density profiles of NGC 3351. The layout is the same as in Figure 2.

are best described as super-fast bars (ZB07, BZ09) of a dumb-bell shape with their thick ends created by the different pattern speeds interacting in the region of their encounter (see also the classification in Appendix B). As we noted in section 1, super-fast bars are an unexpected finding that has come out of the application of the phase shift method, because they contradict the results of passive orbit analyses that imply that a bar cannot extend beyond its own CR due to a lack of regular orbital support (Contopoulos 1980).

2.1.2. NGC 3351 (M95)

NGC 3351 (M95) is a barred spiral galaxy of MIR RC3 type (R')SB(r,nr)a (Buta et al. 2010). It lies at a distance of approximately 10 Mpc. In spite of the early-type classification, the galaxy has a very small bulge. Its actual bulge, in the form of a bright nuclear ring, is regarded as a pseudobulge by Kormendy (2012).

The surface densities of the different mass components for this galaxy derived using IRAC, SDSS, BIMA SONG and THINGS data are shown in Figure 4. Phase shift analyses for NGC 3351 were carried out using the IRAC and SDSS mass surface density images based on the $3.6\mu\text{m}$ SINGS and *i*-band SDSS images, plus the gas maps (Figure 5, top). The phase shift distributions for both the IRAC and SDSS total mass maps show a major CR near $r = 86''$, and also another CR at $r = 26''$.

Figure 5, bottom shows the two CR radii as solid circles superposed on the *g*-band image. Two prominent N/P crossings follow these CR radii at $65''$ and $128''$. For comparison, the inner ring of NGC 3351 has dimensions of $71'' \times 67''$ and lies close to the first N/P crossing, implying that the ring/spiral is a separate mode whose CR is CR₂ at $86''$. In Figure 5, top also, the ex-

tent of the main part of the bar is indicated, and both mass maps show the same thing: the phase shifts are negative across the main part of the bar, implying (as discussed in ZB07 and BZ09) that the corotation radius of the bar is CR₁, not CR₂. Thus, NGC 3351 is also a case of a super-fast bar.

The inner pseudoring at the location of the first major N/P crossing would, in passive orbit analysis in a galaxy with a bar and non-self-gravitating clouds, be considered an inner 4:1 resonance ring as identified by Schwarz (1984) and Buta & Combes (1996). This ring would be directly related to the bar and have the same pattern speed as the bar. Our phase shift analysis, however, suggests that the apparent ring/pseudoring could be due to a “snow plough” effect of two sets of inner/outer patterns having different pattern speeds, and which thus accumulate mass at that radius. The strong and symmetric arms which end a little within the second CR circle might be related to what Contopoulos and collaborators had advocated: that symmetric patterns sometimes end at the inner 4:1 resonance (counterexamples are discussed by ZB07 and BZ09). The spiral patterns outside the second CR circle in this case are more fragmented. It is not yet clear what different dynamics would make some spirals extend all the way to OLR and others end mostly within CR or inner 4:1. Empirical evidence so far shows that those galaxies that have CRs intersecting the arms (such as NGC 5247 analyzed in ZB07) tend to be Sb, Sc or later types, such that the arms are going through the transitional phase from a skewed long inner bar to either a bar-driven spiral or an inner organized spiral plus outer diffused arms. Therefore, the ones where the spiral ends at the inner 4:1 resonance or CR (i.e. the NGC 3351 type) should tend to be the more mature and more steady types, i.e., in earlier-type disks compared to those that have arms being crossed by the CR circle.

2.1.3. NGC 5194 (M51)

NGC 5194 (M51) is a well-known interacting grand design spiral, of MIR RC3 type SAB(rs,nr)bc (Buta et al. 2010). It lies at a distance of approximately 8.4 Mpc. The surface densities of the different mass components for this galaxy derived using IRAC, SDSS, BIMA SONG and THINGS data are shown in Figure 6. It can be seen that the hot dust-corrected total $3.6\mu\text{m}$ surface density profile and that from the *i*-band data are very similar.

The potential-density phase shift method was used to derive the main CR radii for this galaxy (Figure 7). By focusing on the area that just excludes the small companion NGC 5195, which is likely to lie outside

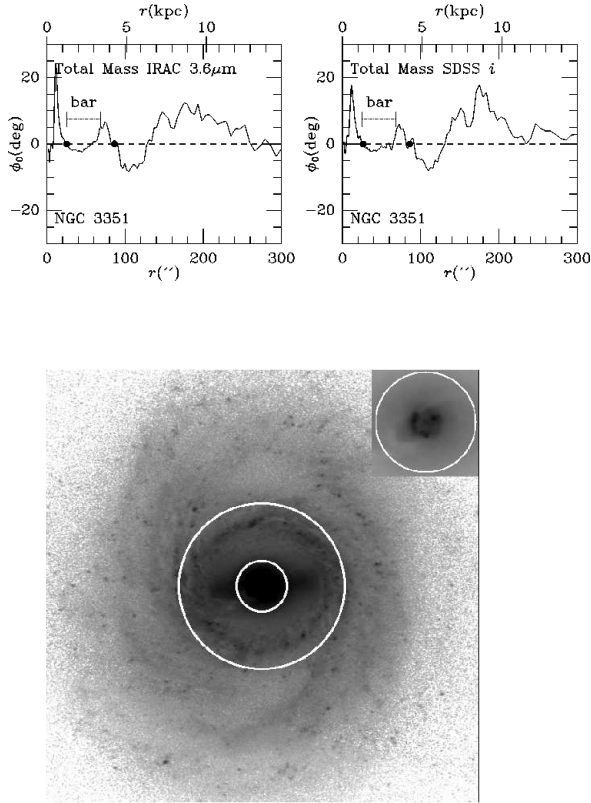


Figure 5: *Top*: Potential-density phase shift versus galactic radius for galaxy NGC 3351 derived using the total mass map with IRAC and SDSS data. *Bottom*: Deprojected g -band image of NGC 3351 in units of mag arcsec^{-2} , with major phase shift crossings superposed as solid circles. The main frame covers an area 7.5 square, while the inset is 0.93 square.

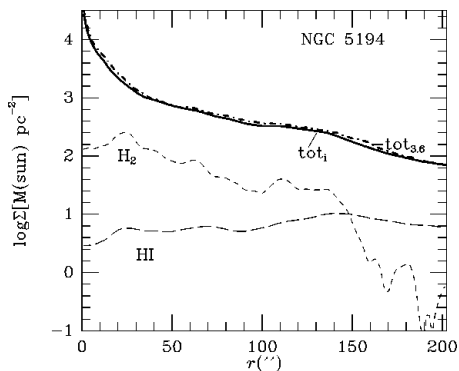


Figure 6: Azimuthally-averaged surface mass density profiles of NGC 5194. The layout is the same as in Figure 2.

of the M51 galactic plane and thus have minor influence on the internal dynamics of M51 at the epoch of observation (a conjecture which was subsequently confirmed), the phase shift analysis gives two major CR radii (P/N crossings on the phase shift plot, represented by solid circles on the overlay image) followed by two negative-to-positive (N/P) crossing radii (not shown on the overlay). The latter are believed to be where the inner modes decouple from the outer modes. The CR radii, at $21'' \pm 3''$ and $110''$ (Table 2), match very well the galaxy morphological features (i.e., the inner CR circle lies near the end of an inner bar/oval, and the first N/P crossing circle [$r=30''$] is where the two modes decouple). Also, for the outer mode, the CR circle seems to just bisect the regions where the star-formation clumps are either concentrated on the inner edge of the arm, or on the outer edge of the arm, respectively – a strong indication that this second CR is located very close to where the pattern speed of the wave and the angular speed of the stars match each other (this can be compared to a similar transition of arm morphology across the CR in a simulated galaxy image of Z96, Fig. 3). This supports the hypothesis that the spiral patterns in this galaxy are intrinsic modes rather than being tidal and transient. Tidal perturbations in this case serve to enhance the *prominence* of the intrinsic mode, but do not alter its modal shape.

2.1.4. NGC 3627 (M66)

The intermediate-type barred spiral galaxy NGC 3627, of MIR RC3 type SB(s)b pec (Buta et al. 2010), is a member of the interacting group the Leo Triplet (the other two members being NGC 3628 and NGC 3623). It lies at a distance of approximately 10 Mpc. The surface densities of the different mass components for this galaxy derived using IRAC, SDSS, BIMA SONG and THINGS data are shown in Figure 8. As for NGC 3351, 4321, and 5194, the total $3.6\mu\text{m}$ mass profile and the total i -band mass profile are in good agreement over a wide range of radii.

Zhang, Wright, & Alexander (1993) observed this galaxy in high-resolution CO(1-0) and HI, and found that the choice of an outer CR location at $220''$ coinciding with the outer HI cutoff could account for many observed morphological features. Subsequent observations, e.g. those of Chemin et al. (2003) in the $H\alpha$ line, determined that an inner CR enclosing the central bar is a more reasonable choice. Our new surface density map allows us to re-evaluate the question of CR determination for this galaxy, bearing in mind that the PDPS method gives the most reliable CR determination only for potential-density pairs that have achieved dynamical

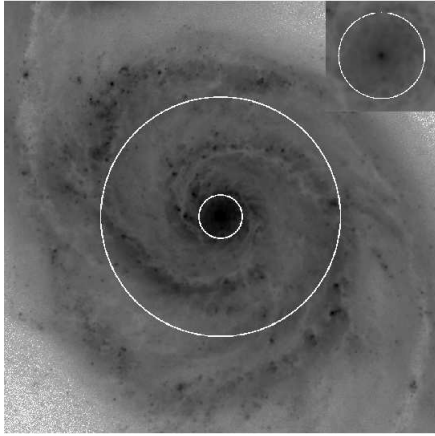
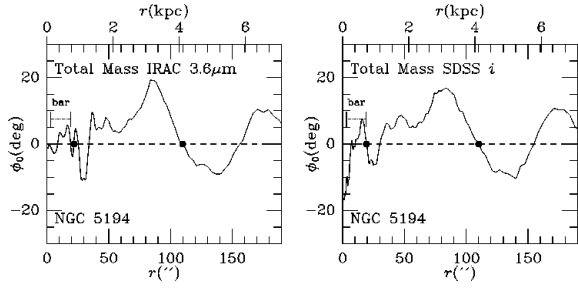


Figure 7: *Top*: Calculated phase shift vs galaxy radii for NGC 5194 (M51) using the IRAC data as well as SDSS data. Two corotation radii (filled circles) are indicated. *Bottom*: CR circles overlaid on the deprojected *g*-band image of NGC 5194 (M51). The main frame covers an area $6'.6$ square, while the inset is $0'.93$ square. The units are mag arcsec^{-2} .

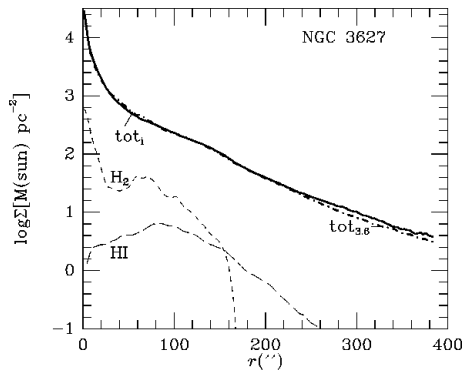


Figure 8: Azimuthally-averaged surface mass density profiles of NGC 3627. The layout is the same as in Figure 2.

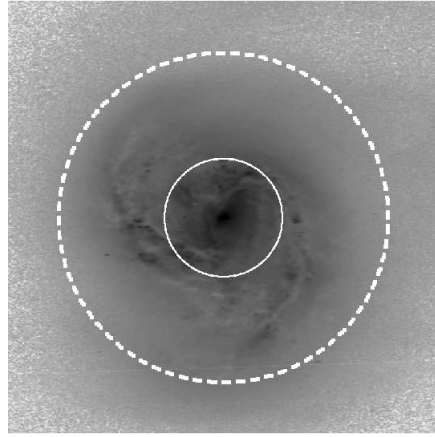
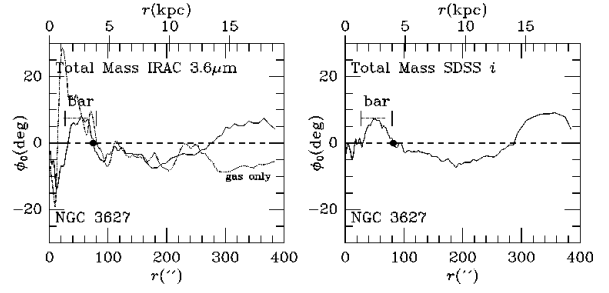


Figure 9: *Top*: Calculated phase shifts between the stellar mass and total potential, and the HI gas mass and the total potential, for NGC 3627. *Bottom*: Overlay of CR circles on the *g*-band image for NGC 3627. The main frame covers an area $9'.6$ square. The units are mag arcsec^{-2} .

equilibrium, a condition which is likely to be violated for this strongly-interacting galaxy that has suffered serious damage in its outer disk (e.g., Fig. 1 of Zhang et al. 1993).

In Figure 9, top, we show the phase shifts with respect to the total potential of the total mass distribution, as well as for the total gas distribution. The total mass phase shifts display only one inner CR at $78''.6 \pm 3''.5$, which can be compared to the CR radius obtained by Chemin et al. (2003) of $\sim 70''$, yet the large-radius phase distribution shows clear evidence of the disturbance caused by the interaction, and thus (by implication) a lack of dynamical equilibrium for this galaxy. The main CR appears to encircle the bar ends in NGC 3627 (Figure 9, bottom), which would make the galaxy a “fast bar” case according to BZ09 (see also Appendix B).

The total gas phase shift shows the presence of a second possible CR between $220''$ - $260''$, close to the one adopted in Zhang et al. (1993) of $220''$. The ra-

dius of this possible CR is ill-defined since the phase shift barely reaches zero and does not become a clear P/N crossing. Figure 9, bottom, shows the g -band image overlaid with the two possible CR circles, selecting $220''$ for the outer CR as the minimum likely value. The total mass map shows two faint outer arms that extend towards the outer CR circle – in fact these outer spiral arms extend much further than the impression given in the g -band image, as can be seen in the non-deprojected HI surface density profile (Zhang et al. 1993, Figure 7; as well as a similar HI image on the THINGS website).

According to the one-CR view of Chemin et al. (2003), the main spiral would be bar-driven. However, this view would be contradicted by the two strong disconnected bow-shocks at the CR circle, indicating the interaction of two pattern speeds (these disconnected bow shock segments in fact show up more clearly in the gas surface density map). Truly bar-driven spirals do not contain these disconnected bow-shock segments, and the spirals would appear as the further continuation of a skewed bar (see Appendix B). The outer spiral arms in the case of NGC 3627 clearly do not connect smoothly with the inner bar – in fact, there is evidence of two sets of spiral patterns, the inner set with short arms appears bar-driven whereas the outer set is offset in phase in the azimuthal direction from the inner one.

With this additional evidence, we propose that prior to the encounter with NGC 3628, NGC 3627 originally had a two-pattern structure similar to the CR₃ and CR₄ regions of NGC 4321. The interaction tore out a large part of the outer surface density from NGC 3627, including a segment of the outer spiral arm (Zhang et al. 1993, Figure 5, clump L). Therefore the galaxy is evolving towards a new dynamical equilibrium, with the possibility of losing the coherent outer spiral pattern eventually.

2.1.5. NGC 628

NGC 628 is a late-type spiral of MIR RC3 type SA(s)c (Buta et al. 2010). It lies at a distance of 8.2 Mpc. The surface densities of the different mass components for this galaxy derived using IRAC, BIMA SONG and THINGS data are shown in Figure 10. For this galaxy, no SDSS data are available. Unlike the other galaxies in our sample, NGC 628 (due partly to its late morphological type) has considerable HI gas at large radii, and this accounts for the significant departure of the total mass profile from the stellar density profile alone.

The phase shift plot (Figure 11, top) shows noisier organization compared to all the other galaxies in this sample, which is consistent with this galaxy being of

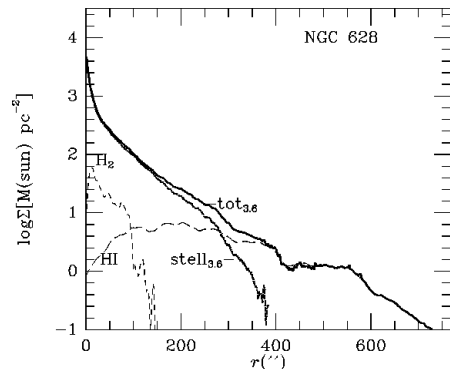


Figure 10: Azimuthally-averaged surface mass density profiles of NGC 628. The HI and H₂ profiles are shown, and the stellar and total mass profiles based on a $3.6\mu\text{m}$ image.

very late type (Buta & Zhang 2009). In the secular evolution picture this corresponds to a young pattern still in the process of settling down towards a dynamical equilibrium state. Nevertheless, there are indications of four P/N crossings which are represented by the filled circles in the figure. Table 2 lists the radii of these crossings. Figure 11, bottom, shows the overlay of CR circles on a deprojected B -band image of NGC 628.

2.1.6. NGC 4736

NGC 4736 is an early-type spiral of MIR RC3 type (R)SAB(rl,nr',nl,nb)a (Buta et al. 2010), implying a galaxy with many distinct features. It lies at a distance of about 5 Mpc. In addition to the usual maps with color-dependent mass-to-light ratio scalings, we have also derived a map using the SDSS i -band image and the mass-to-light profiles obtained through a fitting procedure by Jalocha et al. (2008). This is because the usual color-based approach gives a stellar surface density distribution that leads to a predicted rotation curve much higher than the observed rotation curve in the central region of the galaxy. We have not made further correction to account for the fact that Jalocha et al. used the Cousins I -band whereas we are using the SDSS i -band, since we expect the uncertainties in the M/L determination would be larger than these differences. The surface mass density curves for this galaxy are shown in Figure 12. The $\text{tot}_{3,6}$ and tot_i curves were derived in the same manner as for the other galaxies. The tot_i (Jal.) profile is based on the purely radius-dependent M/L from Jalocha et al. (2008).

The phase shift derived using the total mass map and the overlay of CR circles on the image is given in Figure 13. The phase shift plot (Figure 13, top) shows sev-

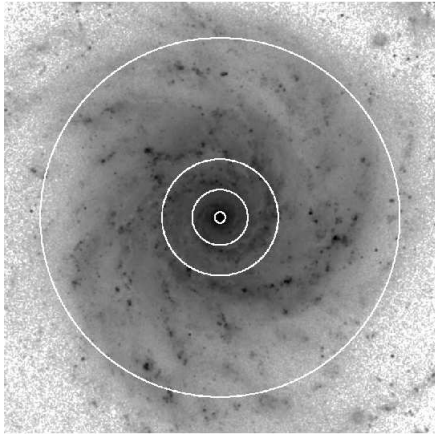
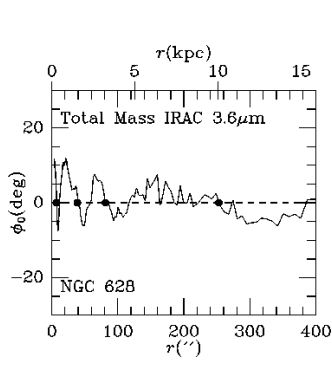


Figure 11: *Top*: Phase shift between the total mass surface density and total potential for NGC 628. *Bottom*: Deprojected *B*-band image of NGC 628 overlaid with CR circles. The main frame covers an area 10.1 square. The units are mag arcsec^{-2} .

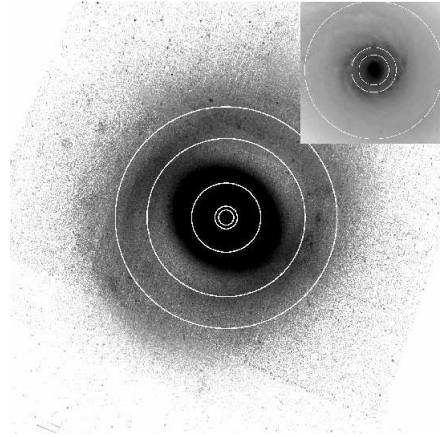
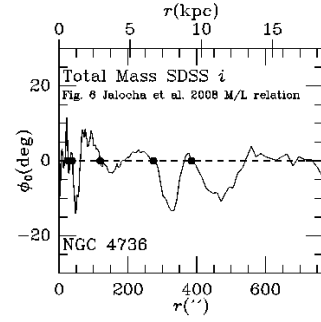


Figure 13: *Top*: Phase shift between the total mass surface density and total potential for NGC 4736, derived using the SDSS data. *Bottom*: SDSS *g*-band image of NGC 4736 with the CR circle overlay. The main frame covers an area 25.4 square, while the inset has an area 4.25 square. The units are mag arcsec^{-2} .

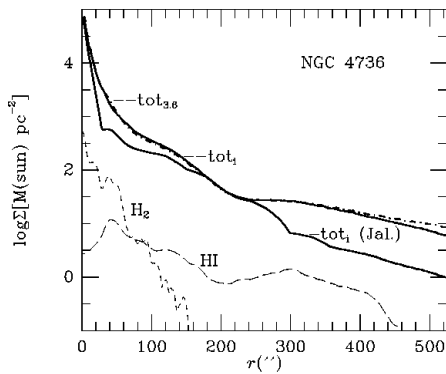


Figure 12: Azimuthally-averaged surface mass density profiles of NGC 4736. The layout is the same as in Figure 2, except that graph includes the profile scaled according to the mass-to-light ratio profile used by Jalocha et al. (2008).

eral well-delineated P/N crossings (Table 2) which appear to correspond well to the resonant structures in the image (Figure 13, bottom). CR₁ could be associated with an inner nuclear bar, while CR₂ is a mode associated with the bright spiral inner pseudoring. CR₃ could be associated with an intermediate spiral pattern outside the prominent inner ring. The fact that CR₄ passes through the gap between the inner and outer rings suggests that it is the actual CR of the massive oval. CR₅ may be associated with the outer ring pattern.

2.2. Rotation Curves and Secular Mass Flow Rates

In the next group of figures (Figure 14 and Figure 15), we present the rotation curves (observed versus disk-total-mass-derived) as well as the total mass flow rates for our sample galaxies. The arrangement of the different frames, NGC 628, NGC 4321, NGC 5194, NGC 3627, NGC 3351, NGC 4736, from left to right, then top to bottom, is chosen to be roughly along the Hubble sequence from late to early types, in order to reveal any

Table 2: Corotation radii from potential-density phase shifts

Galaxy	CR ₁ (arcsec)	CR ₂ (arcsec)	CR ₃ (arcsec)	CR ₄ (arcsec)	CR ₅ (arcsec)	Filters
NGC 628	7.4	39.2	81.5	253.0:	3.6
NGC 3351	26.2±0.4	86.5±5.1	3.6, <i>i</i>
NGC 3627	78.6±3.5	3.6, <i>i</i>
NGC 4321	8.3±0.7	28.8±0.6	51.9±0.0	136.9±1.6	3.6, <i>i</i>
NGC 4736	27	39	120	275	385	<i>i</i>
NGC 5194	21.3±3.1	110.1±0.1	3.6, <i>i</i>

systematic trends along this sequence. Because two of the intermediate types (NGC 5194 and NGC 3627) are strongly interacting galaxies, they might deviate from the quiescent evolution trends. Since there is usually a limited radial range for the availability of observed rotation curves, our subsequent plots in this section (Figures 14-20) will be displayed with smaller ranges than were used for the corresponding phase shift plots.

From Figure 14, we observe that the contribution of the disk baryonic matter (excluding the contribution from helium and heavy elements) to the total rotation curve increases as the galaxy’s Hubble type changes from late to early along the Hubble sequence. For early-type galaxies such as NGC 4736, the entire rotation curve may be accounted for by disk baryonic matter (Jalocha et al. 2008). Note that the close match between the observed and disk-inferred rotation curves for NGC 3627, which is unusual for its intermediate Hubble type, may be a result of the close encounter with NGC 3628 which is likely to have stripped a large portion of its halo.

The mass flow rates obtained from equation 2 are not sensitively dependent on the choice of scale height in the potential calculation (i.e. a factor of 3.3 change of vertical scale height from 12.6” to 3.8” in the case of NGC 4321 changed the scale of mass flow by less than 10% for the entire radial range considered). So the scale heights we used from Table 1 for each individual galaxies should give a fairly good estimate of the mass flow rates. From Figure 15, the mass flow rates for the various Hubble types range from a few solar masses per year to about a few tens of solar masses a year, except for the very late-type galaxy NGC 628 which is still in the process of settling into a significant galaxy-wide mass flow pattern. The intermediate-type galaxies appear to have the largest mass flow rates (e.g., NGC 1530, studied in ZB07, has mass flow rates on the order of 100 solar masses a year and is also an intermediate-type galaxy), whereas for the early-type galaxies the mass flow is more concentrated to the central region.

The averaged radial flow velocities $v_R(R)$ corresponding to the averaged mass flow rates $dM/dt(R)$ displayed in Figure 15 can be obtained by dividing the mass flow rate dM/dt by $2\pi R\Sigma_0$, where Σ_0 is the local averaged surface density. This gives a radial velocity typically on the order of a few km/sec. Since the non-circular velocities in a galaxy possessing highly nonlinear density wave patterns can be significantly larger than these radial flow velocities, a direct measurement of the radial flow velocities may not be as reliable a way of estimating the mass flow rate compared to the torque/phase shift approach described here.

Although both inflow and outflow of mass are present at a given epoch across a galaxy’s radial range, there is a general trend for the mass to concentrate into the inner disk with time, together with the build-up of an extended outer envelope, consistent with the direction of entropy evolution. This is confirmed in Figure 16, which shows that for late and intermediate-type galaxies the gravitational torque couple (as well as the advective torque couple which has similar shape) has mostly positive values in the inner disk, indicating that the angular momentum is consistently being channeled out of the galaxy. The mass flow and angular momentum channeling progressively moves from the outer disk to the inner disk as a galaxy evolves from late to the early Hubble types.

The radial mass flow rates shown in these curves are the lower bounds on the actual rates in physical galaxies, since the nonaxisymmetric instabilities are expected to result in skewed distributions in parts of the thick-disk and halo as well, and thus result in the radial redistribution of the halo dark matter along with the luminous disk matter. Besides the skewed-pattern induced collective radial mass inflow/outflow, we also expect a small amount of additional inflow due to differential rotation and dynamical friction.

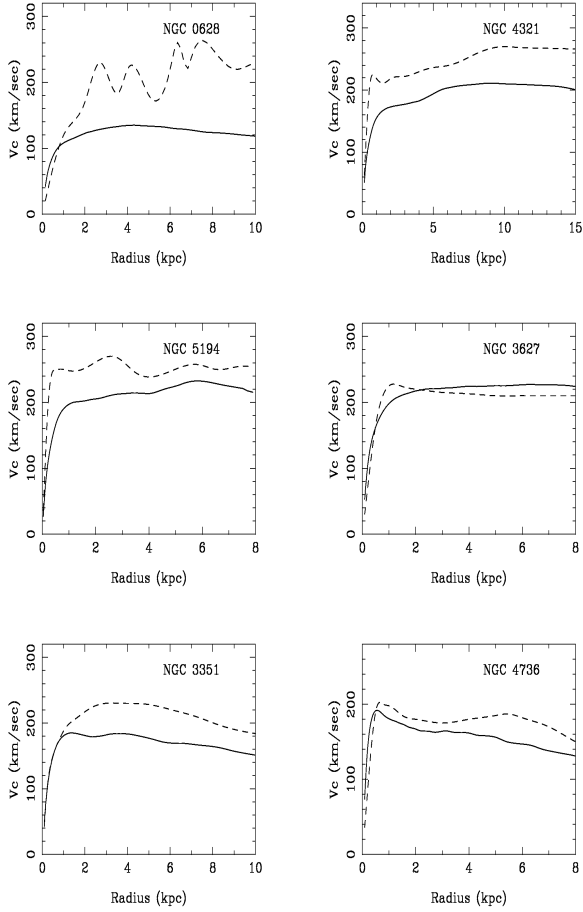


Figure 14: Comparison of rotation curves for the six sample galaxies. *Solid lines*: Disk rotation curves inferred from total disk surface density (stellar plus atomic and molecular hydrogen mass. A very small correction to account for helium and the metal abundance in the gas mass has not been made). The inferred disk rotation curves were derived using IRAC 3.6 μm data for NGC 628, an average of IRAC 3.6 μm and SDSS i-band data for NGC 4321, 3351, 3627, 5194, and using SDSS i-band data for NGC 4736, plus the atomic and molecular gas contribution from the VIVA, THINGS and BIMA SONG observations. *Dashed lines*: Observed rotation curves: NGC 628 - Nicol (2006); NGC 3351 - Inner part from Devereux, Kenney, & Young (1992)'s CO 1-0 observation, outer part from Buta (1988) H-alpha observations; NGC 3627 - Inner part from Zhang et al. (1993)'s CO 1-0 observation (rescaled to the current distance value, and changed to use terminal velocity instead of the peak velocity of the molecular contours), outer part from Chemin et al. (2003)'s H-alpha observation; NGC 4321 - Sofue et al. (1999); NGC 4736 - From Jalocha et al. (2008), adapted from the compilation of Sofue et al. (1999); NGC 5194 (Sofue 1996)

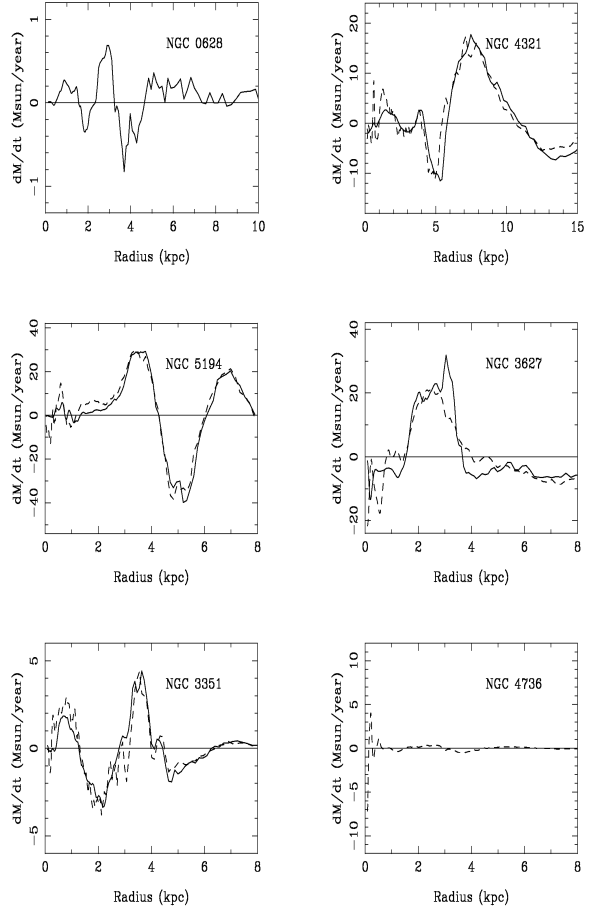


Figure 15: Total radial mass flow rate for the six sample galaxies. Positive portion of the curves indicate inflow, and negative portion of the curves indicate outflow. The solid lines have stellar mass derived from IRAC 3.6 μm data, and the dashed lines have stellar mass derived from SDSS i-band data. Atomic and molecular gas mass from VIVA, THINGS and BIMA SONG were added to obtain the total mass maps which were used to derive these flow rates.

2.3. Relative Contributions from Gravitational and Advective Torque Couples

In Figure 16, we plot the calculated gravitational torque couplings for the six sample galaxies. We note these characteristics:

1. The torque curve for M100 is very similar in shape to the one calculated for the same galaxy by Gnedin et al. (1995), although the scale factor is 10 times smaller than obtained in their paper. Part of the difference can be accounted for from the difference in galaxy images used (i.e. wave bands) and in the galaxy parameters used between these two studies. We have used an R -band image as in Gnedin et al., and rescaled the galaxy parameters to be in agreement with what they had used. However, as was also found by Foyle et al. (2010), after these adjustments the resulting scale still differs by a factor of ~ 5 from that in Gnedin et al. (1995).

2. For most of the galaxies in the sample, C_g has a primary peak which is centered in the middle of the disk, suggesting that the mass inflow/outflow should be focused near the peak location of the main bell curve. This location is expected to change with time for a given galaxy as secular evolution proceeds because the basic state configuration and the resulting modal configuration will both evolve due to the redistribution of the disk mass. By examining this small sample of six galaxies, we can already see a trend that the main peak of the C_g curve moves from the outer region of the galaxy (as for NGC 628) to the mid-disk (as for NGC 4321, 5194 and 3627), and then to the central region (NGC 3351 and 4736).

3. The existence of multiple humps in the gravitational torque couple³ in a single galaxy, and by implication multiple nested modes of differing pattern speeds, shows that the secular mass flow process is *not a one-way street*. During the lifetime of a galaxy a given radial range will experience inflows and outflows of different magnitudes, but there is an overall trend towards a gradual increase of central concentration together with the build-up of an extended envelope, consistent with the entropy evolution direction of self-gravitating systems. Galaxies accomplish this in a well-organized fashion, by first employing a dominant mode across the galaxy's outer disk, and then with more of the modal activity moving towards the central region of a galaxy, by bifurcating the single dominant mode into multiple nested modes.

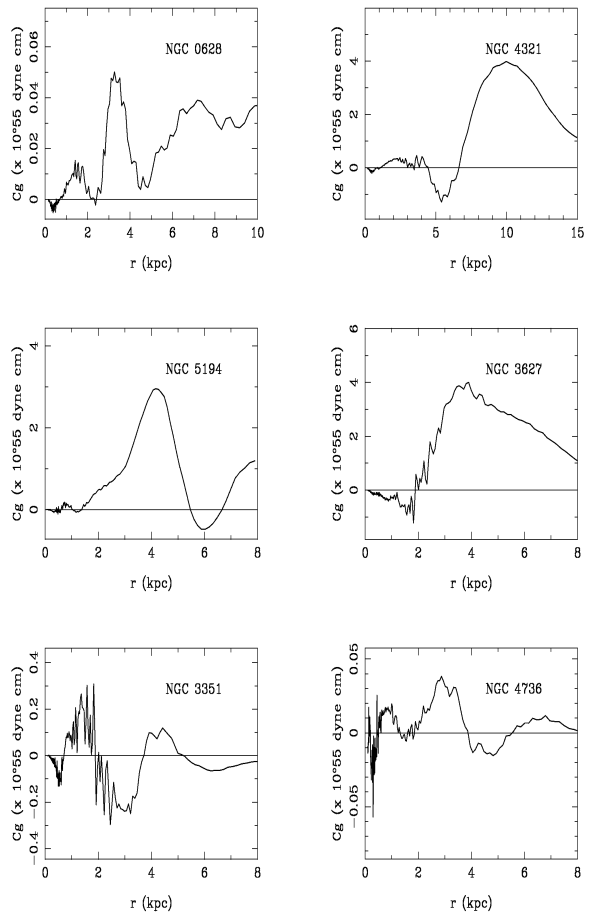


Figure 16: Calculated gravitational torque coupling for the six sample galaxies, using IRAC $3.6 \mu\text{m}$ data for NGC 628, an average of IRAC $3.6 \mu\text{m}$ and SDSS i -band data for NGC 4321, 3351, 5194, 3627, and SDSS i -band data for NGC 4736, to these the usual gas maps were added.

³as well as in the advective and total torque couple, since these latter two are found to be of similar shape to the gravitational torque couple for self-sustained modes

Figure 17 shows the calculated radial gradient of the gravitational torque coupling integral $dC_g(R)/dR$ (dotted curve) as compared to the volume torque integral $T_1(R)$ (solid curve). There is a factor of 3-4 difference between the $T_1(R)$ and $dC_g(R)/dR$ for most of the galaxies in the sample (for NGC 4736, this ratio in the inner region is as high as 8), indicating that the remainder, which is contributed by the gradient of the advective torque coupling, $dC_a(R)/dR$, is in the same sense but much greater in value than $dC_g(R)/dR$. Note that this difference between the volume torque integral and the gradient of the (surface) gravitational torque couple is only expected in the new theory: in the earlier theory of LBK these two are supposed to be equal to each other (e.g., see Appendix A2 of Z98).

Furthermore, if the LBK theory is used literally, one should not expect any mass flow rate at all over most of galactic radii in the quasi-steady state, except at isolated resonance radii (since the total angular momentum flux, $C_a(R) + C_g(R)$, is expected to be constant independent of radius in the LBK theory). The existence of a mass flux across the entire galactic disk, or the multiple peaked-distribution of total torque coupling/angular momentum flux, is thus also contrary to the LBK's original assumption of wave trains in galaxy disks, but is consistent with the conjecture that the patterns in these galaxies are quasi-steady modes. This conjecture is further supported by the fact that we had successfully used the potential-density phase shifts to locate the resonances for the grand-design galaxies in ZB07 and BZ09, which should not have been possible if most of these patterns were transient wave trains. Without the modal nature of the patterns one should not expect to be able to use the mass distribution alone to determine a quasi-kinematic quantity like the corotation radius.

We have also experimented with using the $m=2$ component only to calculate phase shift and mass flow rates, and have compared the results of these calculations with those based on all Fourier modes (i.e., using the full torque expression of equation 2). For most of the grand-design galaxies in our sample, the $m=2$ component makes a dominant contribution in these calculations, which further confirms the modal nature of these observed grand-design patterns (in N-body simulations, whenever a transient feature appears, the $m=2$ torque calculation and the full torque calculation would differ drastically).

We have repeated the calculations for $dC_g(R)/dR$ and $T_1(R)$ using different scale height values. Even though both of these quantities are affected by a particular choice of the scale height, the ratio between the two appears little affected. This is likely due to the fact that the

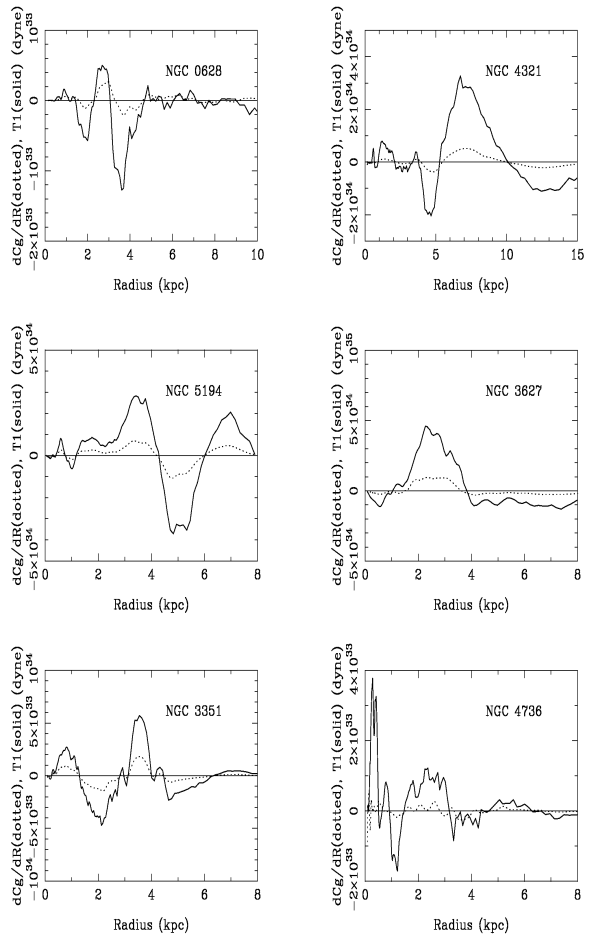


Figure 17: Radial gradient of gravitational torque coupling integral compared with the volume torque integral for the six sample galaxies. For NGC 628, used IRAC 3.6 μm data; for NGC 4321, 3351, 3627, 5194, used the average of IRAC 3.6 μm and SDSS i-band data; for NGC 4736, used SDSS i-band data; to these the usual gas maps were added.

potential that is being affected by the scale height choice enters into both the C_g and the $T_1(R)$ expressions, so their ratio is less sensitive to the choice of scale height. Therefore, our conclusion that there is a significant difference between these two quantities at the nonlinear regime of the wave mode is robust.

2.4. The Relative Contributions of Stellar and Gaseous Mass Flows

In the past few decades, related subjects of secular evolution, bulge growth, and the morphological evolution of galaxies along the Hubble sequence were studied mainly within the framework of the secular redistribution of the gas (interstellar medium) components under the influence of a barred potential, and the resulting growth of the so-called “pseudobulges” (Kormendy 2012 and references therein = K12). Through gas accretion alone, a galaxy could at most build late-type pseudobulges, but not intermediate and early type bulges. This is because the observed gas inflow rates and nuclear star-formation rates are both insufficient to account for the formation of earlier-type bulges through the secular inflow of gas, and the subsequent conversion of gas to stars during a Hubble time (K12). Yet observationally, early type galaxies (including disk-Es) are known to form a continuum with the intermediate and late-type disk galaxies, in terms of their structural parameters, kinematics, and stellar populations (Jablonka, Gorgas, & Goudfrooij 2002; Franx 1993; Cappellari et al. 2013), and thus their formation and evolution mechanisms are also expected to form a continuous trend.

With the recognition of the role of collective effects in the secular mass redistribution process, the study of secular morphological transformation of galaxies should now give equal emphasis to the roles of stellar and gaseous mass redistribution. Due to their different intrinsic characteristics (radial surface density distribution, compressibility, star-formation correlation, and dissipation capability), stars and gas do play somewhat different roles in the secular evolution process. In this subsection we illustrate with our sample galaxies some of the specifics of these roles.

In Figure 18 and 19, we present the comparison of stellar and gaseous (HI plus H₂) mass flow rates, as well as their respective phase shifts with respect to the total (star plus gas) potential. The phase shift plots tell us the relative efficiency of the stellar and gaseous mass accretion processes, since the angular momentum exchange rate between the disk matter and the density wave, per unit area, can be written as (Z98, equation 25)

$$\frac{dL}{dt}(R) = \frac{1}{2} F^2 v_c^2 \tan i \sin(m\phi_0) \Sigma_0, \quad (6)$$

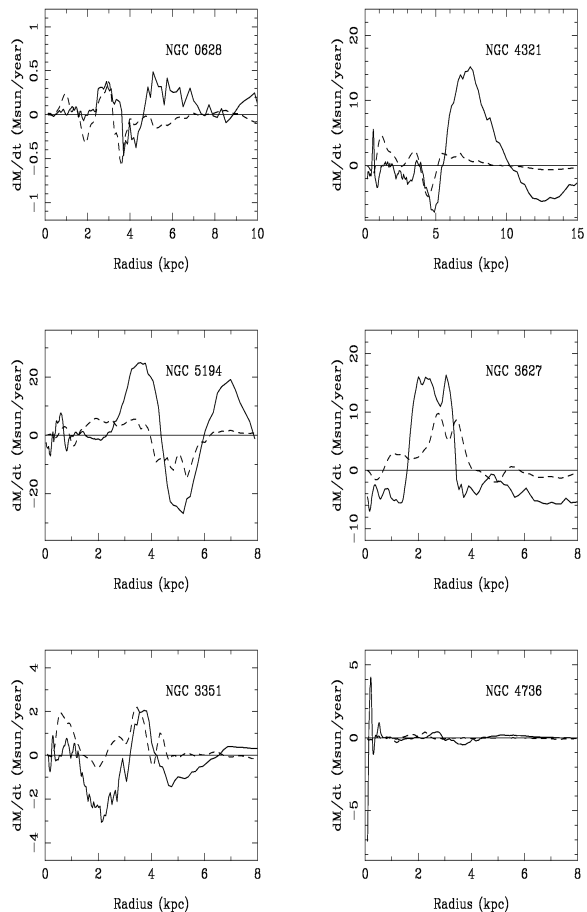


Figure 18: Stellar and gaseous mass flow rates for the six sample galaxies, calculated from the IRAC 3.6 μm for NGC 628, an average of IRAC 3.6 μm and SDSS i-band for NGC 4321, 5194, 3627, 3351, and SDSS i-band for NGC 4736, plus VIVA, THINGS and BIMA SONG data. The total potentials used for these calculations were the same as previously derived using IRAC and/or SDSS for the stellar contributions, with appropriate averaging, plus the gas contributions.

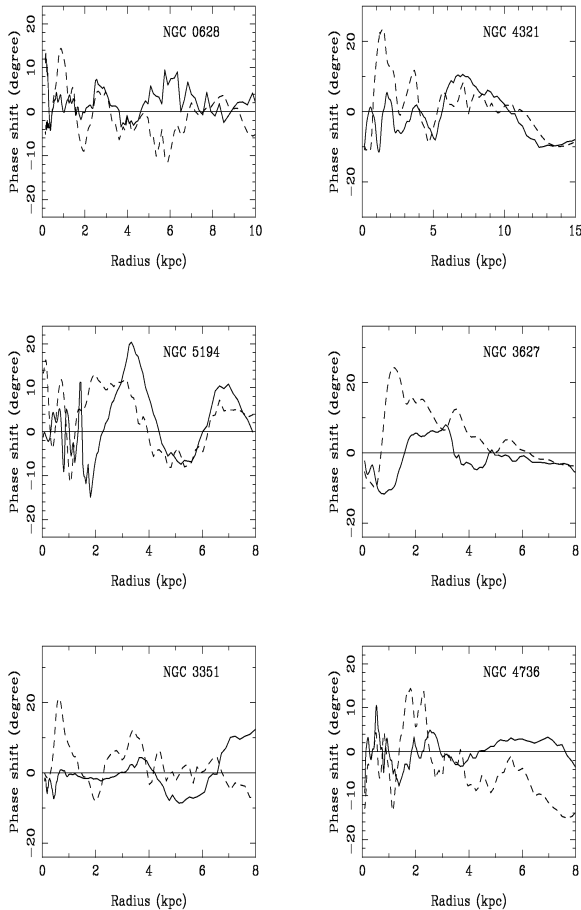


Figure 19: Stellar and gaseous phase shift with respect to total potential for the six galaxies. *Solid lines*: Stellar phase shifts. *Dashed lines*: Gaseous phase shifts. The stellar maps were derived using the IRAC $3.6 \mu\text{m}$ data for NGC 628, using an average of IRAC and SDSS data for NGC 4321, 3351, 3627, 5194, and using SDSS i-band data for NGC 4637. The maps were from VIVA, THINGS and BIMA SONG observations. The total potentials used for these calculations were the same as previously derived using IRAC and/or SDSS for the stellar contributions, with appropriate averaging, plus the gas contributions.

where $F^2 \equiv F_\Sigma F_\gamma$ is the product of the fractional density and potential wave amplitudes, and m is the number of spiral arms (usually taken to be 2). Therefore, using the previously derived mass flow rate equation (2) and volume torque expression equation (5), which applied for the unit-width annulus rather than per unit area, we have

$$\sin(m\phi_0)_i = \frac{1}{\pi v_c R F_i^2 (\Sigma_0)_i} \frac{dM_i}{dt} \quad (7)$$

where the subscript i represents stars or gas, respectively. So for similar wave amplitudes between stars and gas, the mass component that has higher phase shift will have higher mass flow rate per unit surface density.

For galaxy NGC 628, the stellar and gaseous accretion efficiencies are similar, as are the respective total mass accretion rates, since this is a late-type spiral galaxy and is gas rich. The alignment of the stellar and gaseous phase shifts is poor, however, especially for the outer disk, indicating that the galaxy is yet to evolve into a state of dynamical equilibrium.

NGC 4321 is relatively quiescent and of intermediate Hubble type. From Figure 19, we see that for much of the central region (except the very center) the gaseous phase shift with respect to their common potential is much larger than the stellar phase shift, indicating that gas leads in phase in this region compared to stars, revealing a higher dissipation rate and mass redistribution efficiency of the gas compared to the stars for the central region of this galaxy. The values of the phase shifts of the stars and gas are comparable for the outer region, indicating that the two mass components have similar mass-redistribution efficiency there. The shapes of the positive and negative humps of phase shifts for stars and gas have more similar radial distributions for this galaxy compared to NGC 628, especially for the outer region, indicating a higher degree of dynamical equilibrium. The overall contribution of the stars to mass redistribution, however, is much higher than for the gas in the outer region (Figure 18), because of the higher overall stellar surface density there.

For NGC 5194 (M51), the stellar and gaseous phase shifts have significantly different radial distributions compared to NGC 4321, even though both galaxies are of intermediate Hubble type. This is likely because of the non-dynamical-equilibrium state of M51 due to the tidal pull of the companion, and the inevitable evolution towards forming a new set of nested resonances, with the gas playing a leading role in seeking the new dynamical equilibrium because of its more dissipative nature, and the stellar component lagging somewhat be-

hind in this action. But at every moment of this re-establishment of the dynamical equilibrium, the overall density (i.e. the sum total of stellar and gaseous) still has a much more coherent phase shift distribution with respect to the total potential than each component considered separately (i.e. compared to Figure 7). The overall mass flow rate of stars is much higher than gas for this galaxy.

For NGC 3627, even though the phase shift in the central region shows that gas has a higher accretion efficiency than stars, the overall accretion rate of stars much exceeds that of the gas. The second CR location is not shown here because of the more limited radial range plotted, but is present in the total gas phase shift curve when examined further outward.

For NGC 3351, we see that the central region gas-star relative phase shift is even more prominent than for NGC 4321. This is likely due to the fact that the straight bar potential in the central region of this galaxy is mostly contributed by stars, which has small phase shift with respect to the total potential, and gas thus contributes a much larger phase shift (through its dissipation in the bar potential and the phase offset of its density peak from the stellar density peak) to the overall potential-density phase shift. The overall mass flow rates are contributed similarly by stars and gas for this galaxy. Note that the somewhat chaotic appearance of phase shifts in the outer regions of this galaxy is due to the low surface density there, and thus noise begins to dominate.

For NGC 4736, gas leads stars in parts of the radial range, but the overall contribution to the mass flow is mostly due to stars, especially for the central region, due to the fact that in this early-type galaxy the stellar surface density much exceeds that of the gas. Once again the low surface density in the outer disk of this early type galaxy leads to the more chaotic phase shift distribution there.

We see from this set of plots that one of the old myths of galactic studies, that the gas always torques stars inside and outside CR in the right sense (i.e. that gas should lead stars in azimuth inside CR, and vice versa outside CR), is only true in a small number of instances. To obtain a reliable CR estimate, one really needs to use the total density (stars plus gas) and total potential, and calculate the phase shift zero crossings between these two components to determine the CR locations. In the absence of the gas surface densities, stellar surface density alone and the potential calculated from it (as is done in ZB07), come as the next best compromise. Both of these approaches are much more reliable than using the phase shift between the stellar density and gas density

distributions to determine CR.

We also see that in the majority of the galaxies in the local universe, secular mass flow is dominated by the stellar mass redistribution rather than by gas redistribution, unlike what has been emphasized by many of the earlier works on secular evolution. Furthermore, even for the gas accretion in disk galaxies, the mechanism responsible for its viscosity is still the collective gravitational instabilities (through the scattering of gas cloud in the gravitational potential, which has encounter mean-free-path on the order of a kpc, and the net effect of which manifests as the phase shift between the gas density and the total potential), rather than the microscopic gaseous viscosity due to the collision of gas particles, which has molecular mean-free-path that was long known to be inadequate both for the accretion phenomenon needed to form young stars, and for the accretion phenomenon observed in the gaseous disks of galaxies – thus the well-known need for anomalous viscosity in generalized accretion disks (Lin & Pringle 1987). Z99 showed that the large-scale density wave-induced gravitational viscosity is likely to be the source of anomalous viscosity in both the stellar and gaseous viscous accretion disks of galactic and stellar types.

2.5. *The Relative Contributions of Atomic and Molecular Mass Flows*

In Figure 20, we present the comparison of HI and H_2 mass flow rates for our six galaxies. It is seen that for all six galaxies the H_2 mass flow follows more closely the stellar mass flow distributions, whereas the HI has a more smooth and gradual distribution. This is likely to be a result of the process of the formation of molecular gas (as well as the formation of molecular clouds and complexes) at the spiral arms due to the density wave shock, and their subsequent dissociation. The HI gas distribution, on the other hand, follows a more quiescent dynamics, even though a mild correspondence to the density wave patterns can be discerned.

We emphasize that these plots should not be read as that the HI gas is less responsive to the gravitational perturbation of the density wave than H_2 , but rather that where the response of the gas happens in the spiral shock is also where HI is converted to H_2 , so the responsiveness will show up more prominently in H_2 than in HI .

3. DISCUSSION: IMPLICATIONS ON THE SECULAR MORPHOLOGICAL TRANSFORMATION OF GALAXIES

In the results presented so far, a picture emerges of the secular morphological transformation of galaxies driven mostly by collective effects mediated by large-scale density wave modes. This evolution will slowly change the basic state mass distribution towards that of an ever increasing central (bulge) mass together with the build-up of an extended outer envelope. These changes are accompanied by a corresponding change in the morphology, kinematics, and other physical properties of the density wave modes (including the formation of successive nested resonances), so at every stage of the transformation from the late to the early Hubble types, there should be a good correspondence between the basic state properties and the density wave modes. Once the galaxy has settled onto an initial quasi-steady state, as it transforms its morphology from late to intermediate Hubble types, only during brief periods in its subsequent life, when it encounters gravitational perturbation from a companion galaxy, such as the case for M51 or NGC 3627, will the coherence of its phase shift curve and its kinematic and dynamical equilibrium be temporarily disturbed. A new equilibrium state is expected to be restored once the perturbation ceases and the galaxy adjusts its mass distribution and modal pattern to be once again mutually compatible. The reason these new equilibrium states are always possible is because for every commonly-occurring basic state configuration there is almost always a set of unstable modes corresponding to it (Bertin et al. 1989).

As a result of this coordinated co-evolution of the basic state of the galaxy disk and the density-wave modes it supports, over the major span of a galaxy's lifetime the effective evolution rate depends on the stage of life a galaxy is in. Late- or intermediate-type galaxies, having larger equilibrium amplitude and open-spiral/skewed-bar modes in their outer disks, would lead to larger mass flow rates and thus higher secular evolution rates in the outer disk. In contrast, for early type galaxies, the secular evolution activity is shifted to the central region of a galaxy, and in its outer region the tightly-wrapped spirals or more straight bars both lead to small potential-density phase shifts and low mass flow rates.

The secular evolution rate also depends on the interaction state of a galaxy, with a galaxy in group or cluster environments generally having larger evolution rates due to the large-amplitude, open spiral and bar patterns excited (Zhang 2008). Interaction-enhanced, density-wave mediated evolution appears to underlie the so-

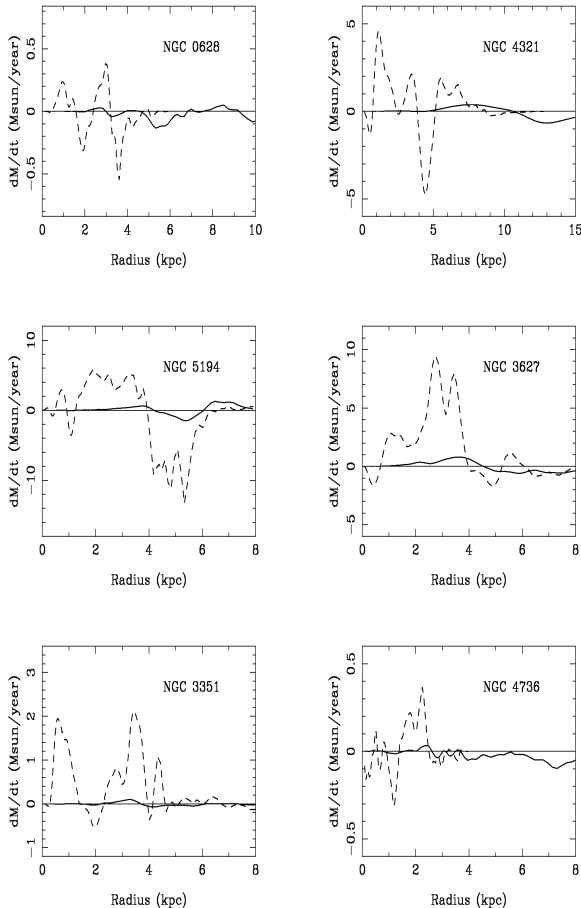


Figure 20: HI and H_2 mass flow rates for the six sample galaxies. *Solid lines*: HI mass flow rates. *Dashed lines*: H_2 mass flow rates. The HI mass flow rates were derived using mass maps from VIVA and THINGS observations, and H_2 flow rates were derived using mass maps from BIMA SONG observations. The total potentials used for these calculations were the same as previously derived using IRAC and/or SDSS for the stellar contributions, with appropriate averaging, plus the gas contributions.

called morphological Butcher-Oemler effect (Butcher & Oemler 1978) in rich clusters. Furthermore, there is the well-known morphology-density relation (Hubble & Humason 1931; Dressler 1980), which has been shown by various teams to hold over more than 4 orders of magnitude in mean density spanning environments from small field groups, to poor clusters, to rich-cluster outskirts, all the way to dense cluster central regions. The universality of such a correlation is in fact a powerful illustration of the unifying role played by “nurture-assisted-nature” type of processes during galaxy evolution. On the other hand, as we see in the current work, even for strongly interacting galaxies such as M51 and NGC 3627, the environment exerts its effect through the innate mechanism already present in individual galaxies: the density wave patterns that are excited during the interaction are still the intrinsic modes, the effect of interaction having only enhanced the amplitudes of these modes.

The flip side of this correlation of evolution rate with environment is that some disk galaxies in isolated environments could have a very small secular evolution rate throughout the span of a Hubble time, which explains the observational fact that many disk galaxies in the field are found to have evolved little during the past few Gyr (essentially, this is why we still observe disk-dominated galaxies in the nearby universe at all, instead of all galaxies having evolved into bulge-dominated configurations). Still, an isolated environment cannot be automatically equated to a slow evolution rate. One of the most impressive examples of a strongly excited density wave pattern we have encountered is in the SB(s)b galaxy NGC 1530 (ZB07), which lies in a surprisingly pristine environment, i.e., nearly totally isolated. Yet NGC 1530 has by far the largest mass flow rate of all the galaxies we have applied the PDPS method to so far, on the order of more than $100 M_{\odot} \text{ yr}^{-1}$, due to its large surface density and the presence of a strong bar-spiral modal structure. This shows that the initial conditions that galaxies inherited at birth are likely to have played an important role as well in determining the subsequent morphological evolution rate.

The secular morphological transformation of galaxies along the Hubble sequence also implies that the required external gas accretion rate to sustain the current level of star formation in disk galaxies can be much reduced from the amount previously sought: As a galaxy’s Hubble type evolves from late to early, more and more of its store of primordial gas will be exhausted, and its star-formation rate will naturally decline. But this is precisely the observed trend of star-formation in galaxies along the Hubble sequence: i.e., the early-type disk

galaxies do not have nearly as much star formation activity as late-type galaxies. Galaxies thus do not have to sustain their “current” level of star formation over cosmic time, since what is current today will be history by the next phase of their morphological evolution.

A further inference is that as galaxies evolve from late to early Hubble types, the central potential well will gradually become deeper, thus more and more nested resonances form in the nuclear region as a result (Zhang et al. 1993). These successive resonances form a continued chain of mass accretion into the central region of a galaxy while the bulge itself grows, and this process could naturally account for the observed correlations between the galaxy bulge mass and central black-hole mass.

Finally, we note that the continuous evolution across the S0 boundary into disk Es may erase the distinction between pseudobulges and classical bulges, i.e., many galaxies of the Milky Way type or earlier were previously thought to have classical bulges because of their $r^{1/4}$ central density profile, yet the building up of these intermediate- to early-type galactic bulges is most likely through the secular mass accretion process over the past Hubble time – provided only that the disk bulges further relaxed into the $r^{1/4}$ shaped bulges with time. In the end, as has already been pointed out by Franx (1993), there might not be a clear distinction between early type disks and disk Es, only a gradual variation of the bulge-to-disk ratio. The recent results from the ATLAS^{3D} project of a significant disk component in all low-mass ellipticals, as well as the structural and population continuity between the early-type disk galaxies and disk ellipticals (Cappellari et al. 2013) also support this continuous evolution trend from late type disk galaxies all the way to disk Es.

4. CONCLUSIONS

We have presented a study of a sample of six galaxies with a broad range of Hubble types in order to obtain an initial estimate of their radial mass accretion/excretion rates, and thus to gauge the relevance of secular mass redistribution processes to the morphological transformation of galaxies along the Hubble sequence. Our results show that the mass flow rates obtained in typical disk galaxies are able to produce significant evolution of their Hubble types over cosmic time, especially if such disk galaxies have undergone external perturbation due to tidal interactions with companion galaxies in a dense environment. We have found that the reasons past studies have often concluded that secular evolution is only important for building up late-type pseudo-bulges are,

first of all, due to the neglect of the important role of stellar mass accretion, and secondly, the neglect of the dominant role played by collective effects enabled by self-organized density wave modes.

REFERENCES

- Bell, E. F. & de Jong, R. S. 2001, *ApJ*, 550, 212
 Bell, E.F., McIntosh, D.H., Katz, N., & Weinberg, M.D. 2003, *ApJS*, 149, 289
 Bertin, G., Lin, C.C., Lowe, S.A., & Thurstans, R.P. 1989, *ApJ*, 338, 78
 Binney, J., & Tremaine, S. 2008, *Galactic Dynamics*, second ed. (Princeton: Princeton Univ. Press) (BT08)
 Buta, R. 1988, *ApJS*, 66, 233
 Buta, R. & Combes, F. 1996, *Fundamentals of Cosmic Physics*, 17, 95
 Buta, R., Corwin, H.G., Jr., de Vaucouleurs, G., de Vaucouleurs, A., & Longo, G. 1995, *AJ*, 109, 517
 Buta, R. & Williams, K. L. 1995, *AJ*, 109, 517
 Buta, R.J., & Zhang, X. 2009, *ApJS*, 182, 559 (BZ09)
 Buta, R. et al. 2010, *ApJS*, 190, 147
 Butcher, H., & Oemler, A., Jr. 1978, *ApJ*, 219, 18; 226, 559;
 Cappellari, M. et al. 2013, *MNRAS*, 432, 1862
 Chemin, L., Cayatte, V., Balkowski, C., Marcelin, M., Amram, P., van Driel, W., & Flores, H. 2003, *A&A*, 405, 89
 Chung, A., van Gorkom, J. H.; Kenney, J.D.P., Crowl, H., Vollmer, B. 2009 *AJ*, 138, 1741
 Contopoulos, G. 1980, *A&A*, 81, 198
 Devereux, N.A., Kenney, J.D., & Young, J.S. 1992, *ApJ*, 103, 784
 de Grijs, R. 1998, *MNRAS*, 100, 595
 Donner, K.J., & Thomasson, M. 1994, *A&A*, 290, 785
 Dressler, A. 1980, *ApJ*, 236, 351
 Eskridge, P.B. et al. 2002, *ApJS*, 143, 7
 Flagey, N., Boulaner, F., Verstraete, L., Miville Deschênes, M. A., Noriega Crespo, A., & Reach, W. T. 2006, *A&A*, 453, 969
 Foyle, K., Rix, H.-W., & Zibetti, S. 2010, *MNRAS*, 407, 163
 Franx, M. 1993, in *Proc. IAUS 153, Galactic Bulges*, eds. H. Dejonghe & H.J. Having (Dordrecht: Kluwer), 243
 Gnedin, O., Goodman, J., & Frei, Z. 1995, *AJ*, 110, 1105
 González, R.A., & Graham, J.R. 1996, *ApJ*, 460, 651
 Gunn, J.E. et al. 1998, *AJ*, 116, 3040
 Haan, S., Schinnerer, E., Emsellem, E., Garcia-Burillo, S., Combes, F., Mundell, C.G., & Rix, H. 2009, *ApJ*, 692, 1623
 Helfer, T. 2003, Thornley, M. D., Regan, M.W., Wong, T., Sheth, K., Vogel, S. N., Blitz, L.; Bock, D.C.-J. *ApJS*, 145, 259
 Helou G. et al., 2004, *ApJS*, 154, 253
 Hernandez. O., Wozniak, H., Carignan, C., Amram, P., Chemin, L., & Daigle, O. 2005, *ApJ*, 632, 253
 Hubble, E. & Humason, M. 1931, *ApJ*, 74, 43
 Jablonka, P., Gorgas, J., & Goudfrooij, P. 2002, *Ap&SS*, 281, 367
 Jalocha, J., Bratek, L., Kutschera, M. 2008, *ApJ*, 679, 373
 Kendall, S., Kennicutt, R. C., Clarke, C., & Thornley, M. 2008, *MNRAS*, 387, 1007
 Kennicutt, R.C. et al. 2003, *PASP*, 115, 928
 Kormendy, J. 2012, in *Secular Evolution of Galaxies, XXIII Canary Islands Winter School of Astrophysics*, J. Falcón-Barroso & J. H. Knapen, Cambridge, Cambridge University Press, p. 1
 Lin, D.N.C., & Pringle, J.E., 1987, *MNRAS*, 225, 607
 Lynden-Bell, D., & Kalnajs, A.J. 1972, *MNRAS*, 157, 1
 Martínez-García, E.E., González-Lópezlira, R.A., Bruzual, A. G. 2009, *ApJ*, 694, 512
 Martínez-García, E.E., González-Lópezlira, R.A., Bruzual, A. G. 2011, *ApJ*, 734, 122
 Meidt, S., et al. 2012, *ApJ*, 744, 17
 Nicol, M.-H. 2006, *MPIA Student Workshop*, http://www.mpia-hd.mpg.de/70CM/3rdworkshop/presentations/Marie-Helene_Nicol_dark_matter_SF_rate.pdf
 Oh, S., de Blok, W.J.G., Walter, F., Brinks, E., & Kennicutt, R.C., Jr. 2008, *AJ*, 136, 2761
 Quillen, A. C., Frogel, J. A., & González, R. 1994, *ApJ*, 437, 162
 Reach, W. T. et al. 2005, *PASP*, 117, 978
 Schwarz, M. P. 1984, *MNRAS*, 209, 93
 Sellwood, J.A. 2011, *MNRAS*, 410, 1673
 Shostak, G.S., van Gorkom, J.H., Ekers, R.D., Sanders, R.H., Goss, W.M., & Cornwell, F.J. 1983, *A&A*, 119, L3
 Shu, F.S. 1992, *The Physics of Astrophysics*, vol. II. Gas Dynamics, (Mill Valley, Univ. Sci. Books)
 Sofue, Y. 1996, *ApJ*, 458, 120
 Sofue, Y., Tutui, Y., Honma, A., Tomita, A., Takamiya, T., Koda, J., & Takeda, Y. 1999, *ApJ*, 523, 136
 Tully, R.B. 1974, *ApJS*, 27, 415
 Walter, F., Brinks, E., de Blok, W.J.G., Bigiel, F., Kennicutt, R.C.Jr., Thornley, M.D., Leroy, A. 2008, *AJ*, 136, 2563
 Worthey, G. 1994, *ApJS*, 95, 107
 York, D.G. et al. 2000, *AJ*, 120, 1579
 Zhang, X. 1996, *ApJ*, 457, 125 (Z96)

- Zhang, X. 1998, ApJ, 499, 93 (Z98)
 Zhang, X. 1999, ApJ, 518, 613 (Z99)
 Zhang, X. 2008, PASP, 120, 121
 Zhang, X. & Buta, R. 2007, AJ, 133, 2584 (ZB07)
 Zhang, X., Wright, M.C.H., & Alexandria, P. 1993, ApJ, 418,100

APPENDIX A. DESCRIPTIONS OF THE PROCEDURES FOR OBTAINING SURFACE MASS DENSITY MAPS

Stellar surface mass density maps can be made from two-dimensional images using surface colors as indicators of stellar mass-to-light ratio (Bell & de Jong 2001). Calibrated surface brightness maps can be converted to units of $L_{\odot} \text{ pc}^{-2}$, and then multiplied by color-inferred M/L values in solar units to give the surface mass density $\Sigma(i, j)$ in units of $M_{\odot} \text{ pc}^{-2}$ at pixel coordinate (i, j) . Thus our approach is two-dimensional and not based on azimuthal averages of the luminosity distribution.

It is widely regarded that the best images to use for mapping stellar mass distributions are infrared images, because these penetrate interstellar dust more effectively than optical images and also because such images are more sensitive to the light of the old stellar population that defines the backbone of the stellar mass distribution. For our study here, we used two principal types of images: (1) an Infrared Array Camera (IRAC) image taken at $3.6\mu\text{m}$ for the *Spitzer Infrared Nearby Galaxies Survey* (SINGS, Kennicutt et al. 2003); and (2) a $0.8\mu\text{m}$ i -band image obtained from the Sloan Digital Sky Survey (SDSS; Gunn et al. 1998; York et al. 2000). The pixel scales are $0''.75$ for the $3.6\mu\text{m}$ images and $0''.396$ for the i -band images. For NGC 3351 and 3627, the i -band images were rescaled to the scale of the $3.6\mu\text{m}$ images. For NGC 5194, the $3.6\mu\text{m}$ mass map was rescaled to the scale of the i -band to insure that the same area is covered on the two images.

Bell & de Jong (2001) give linear relationships between the log of the M/L ratio in a given passband and a variety of color indices in the Johnson-Cousins systems. Bell et al. (2003) give the same kinds of relations for SDSS filters. For the $3.6\mu\text{m}$ images of NGC 628, 3351, 3627, and 5194, we used $B - V$ as our M/L calibration color index, while for M100 we used $B - R$. For the SDSS i -band, we used $g - i$ as our main color. Using different color indices to scale the two base images from array units to solar masses per square parsec means that independent photometric calibrations are used, allowing us to examine effects that might be due to M/L uncertainties or systematics.

The base images we have used have different advantages and disadvantages for mass map calculations. For example, IRAC $3.6\mu\text{m}$ images have the advantages of much greater depth of exposure than most ground-based near-IR images and also they give the most extinction-free view of the old stellar background. Nevertheless, $3.6\mu\text{m}$ images are affected by hot dust connected with star-forming regions and by a prominent $3.3\mu\text{m}$ emission feature due to a polycyclic aromatic hydrocarbon compound that also is associated with star-forming regions (see Meidt et al. 2012). These star-forming regions appear as conspicuous “knots” lining spiral arms in $3.6\mu\text{m}$ images, such that the appearance of a galaxy at this mid-IR wavelength is astonishingly similar to its appearance in the B -band, minus the effects of extinction (e. g., Buta et al. 2010).

The advantages of the SDSS i -band are the high quality of the SDSS images in general (especially with regard to uniformity of background), the reduced effect of star-forming regions compared to the B -band and the $3.6\mu\text{m}$ band, and the pixel scale which is almost a factor of two better than for the $3.6\mu\text{m}$ IRAC band. Nevertheless, extinction at $0.8\mu\text{m}$ is more than 40% of that in the V -band, so i -band images are considerably more affected by extinction than are $3.6\mu\text{m}$ images.

We use the $3.6\mu\text{m}$ and i -band mass maps as consistency checks on our results since neither waveband is perfect for the purpose intended. In practice, the star-forming region problems in the $3.6\mu\text{m}$ band can be reduced using an $8.0\mu\text{m}$ image if available (Kendall et al. 2008). These “contaminants” can also be eliminated using Independent Component Analysis (Meidt et al. 2012) if no $8.0\mu\text{m}$ image is available.

A1. Procedure

SDSS images - Images were downloaded from the SDSS archive using the on-line DAS Coordinate Submission Form. For the large galaxies in our sample, it was necessary to download multiple images per filter to cover the whole object (ranging from 3 for NGC 3351 to 9 for NGC 4736). These were mosaiced, cleaned of foreground and background objects, and then background-subtracted using routines in the Image Reduction and Analysis Facility (IRAF). SDSS images were available for five of the six sample galaxies, excluding NGC 628.

The zero points for the g and i -band images were obtained using information given on the SDSS DR6 field pages. The airmasses x_g and x_i , calibration zero points aa_g and aa_i , and extinction coefficients kk_g and kk_i , were extracted from this page and the zero points appropriate to the main galaxy fields were derived as

$$zp_g = -(aa_g + kk_g x_g) + 2.5 \log(a_{pix} t)$$

$$zp_i = -(aa_i + kk_i x_i) + 2.5 \log(a_{pix} t)$$

where a_{pix} is the pixel area equal to $(0.396)^2$ or $(0.75)^2$ if rescaled to the $3.6\mu\text{m}$ image and t is the integration time of 53.907456s. For the galaxies that were rescaled, we matched the coordinates of the SDSS g - and i -band images to the system of the $3.6\mu\text{m}$ image, which made it necessary to modify zp_g and zp_i to account for the new pixel size. This was done using IRAF routines GEOMAP and GEOTRAN. Foreground stars were selected that were well-defined on all three of the images. GEOMAP gave the rotation, shifting, and scale parameters, while GEOTRAN performed the actual transformations. Before the final transformations, the point spread function (PSF) of the images was checked. If the PSFs of the g - and i -band images were significantly different, the image with the best seeing was matched to the other using IRAF routine GAUSS. For M100, the higher resolution of the SDSS images relative to the $3.6\mu\text{m}$ image was retained.

The next step was to deproject these images in flux-conserving mode. For this purpose, IRAF routine IM-LINTRAN was used with the adopted orientation parameters (see Table 1). When possible, we used kinematic orientation parameters for the deprojections. In the case of NGC 3351, we also used isophotal ellipse fits to deduce these parameters. No photometric decomposition was used for the deprojections; the bulges were assumed to be as flat as the disk.

The SDSS i -band mass map was derived as follows. The absolute magnitude of the Sun was taken to be $M_i = 4.48$ (CNA Willmer), with which the zero point needed to convert i -band surface brightnesses to solar i -band luminosities per square parsec is $zp_{\odot i} = 26.052$. To convert from these units to solar masses per square parsec, Bell et al. (2003) give a simple relationship:

$$\log \frac{M}{L_i} = -0.152 + 0.518(\mu_g - \mu_i)_o$$

where $(\mu_g - \mu_i)_o$ is the reddening-corrected $g - i$ color index. The only correction made was for Galactic reddening. This was judged using information from the NASA/IPAC Extragalactic Database (NED).⁴ Although NED lists extinction in the broad-band Johnson filters like B and V , the extinctions in g and i were not listed at

⁴This research has made use of the NASA/IPAC Extragalactic Database (NED), which is operated by the Jet Propulsion Laboratory, California Institute of Technology, under contract with the National Aeronautics and Space Administration.

the time we did our study. For these, we used the York Extinction Solver (YES; McCall 2004) on the NED website. The actual use of the above equation requires that some account be made of noise, because SDSS images are not as deep as $3.6\mu\text{m}$ images. For our analysis, it is important to use the two-dimensional color index distribution, not an azimuthal average except in the outer parts of the disk where there is little azimuthal structure. Our procedure was to derive azimuthally-averaged surface brightness and color index profiles, and to interpolate colors from these profiles in the outer regions where noise made the actual pixel color too uncertain to be used in the above equation. Smoothing was also used even in intermediate regions. Usually, the colors in the inner regions were used without smoothing, and then annular zones of increasing radius used an $n \times n$ median box smoothing.

The median-smoothed raw i -band counts, $C_i(i, j)$, at array position (i, j) , were then converted to surface mass density $\Sigma(M_{\odot} pc^{-2})$ through

$$\Sigma(i, j) = C_i(i, j) \times 10^{-0.4(zp_i - A_i - zp_{\odot i})} \\ \times 10^{-0.152 + 0.518[\mu_g(i, j) - \mu_i(i, j) - A_g + A_i]}$$

The final SDSS mass maps usually would have left-over foreground stars that had not been removed, or dark spots in areas of star-formation where the color index was affected by too much blue light. These spots were removed using IRAF routine IMEDIT.

3.6 μm Images - The procedure for these is in many respects similar to the procedure used for the SDSS images, except that different color index maps are used and these are not directly linked to the M/L ratio at $3.6\mu\text{m}$. For $3.6\mu\text{m}$ maps, we used $B - V$ or $B - R$ colors where the individual images are calibrated using photoelectric multi-aperture photometry. The sources and error analysis of such photometry, originally used to derive total magnitudes and color indices for RC3, are described in Buta et al. (1995) and Buta & Williams (1995).⁵ The typical uncertainty in the B -band zero point from this approach is 0.017 mag while for V it is 0.015 mag, based on 8-27 measurements. Fewer measurements are available for R -band calibrations from this approach; the uncertainties in these are described by Buta & Williams (1995). The B and V images used were downloaded from the SINGS database webpage. $B - R$ was used only for M100 and is based on images due to B. Canzian from observations with the USNO 1.0m telescope.

⁵A full catalogue of UBV measurements may be found at <http://kudzu.astr.ua.edu/devatlas/revUBV.ecat.txt>.

The surface brightnesses in the $3.6\mu\text{m}$ images were derived using a common zero point of 17.6935, based on the calibration from Reach et al. (2005). IRAC images are in units of MegaJanskys per steradian.

For our study here, we have made a “hot dust correction” to the $3.6\mu\text{m}$ images using a procedure similar to that outlined by Kendall et al. (2008) since all of our galaxies have an $8.0\mu\text{m}$ image available. The first step is to match the coordinate systems of the 3.6 and $8.0\mu\text{m}$ images and then subtract a fraction (0.232) of the $3.6\mu\text{m}$ flux from the $8.0\mu\text{m}$ image to correct the latter for continuum emission (Helou et al. 2004). Then, a fraction $R_{3.6/8.0}$ of the net dust map is subtracted from the $3.6\mu\text{m}$ map to give an image corrected for the hot dust emission. In general this method did improve our mass maps. The factor we used, $R_{3.6/8.0} = 0.059$, is at the low end of the flux ratios found by Flagey et al. (2006) for the Galactic diffuse interstellar medium.

For converting $3.6\mu\text{m}$ surface brightnesses to solar luminosities per square parsec, the absolute magnitude of the Sun was taken to be $M_{3.6} = M_L = 3.27$ for the L -band, which is close to the same wavelength (Worthey 1994). This corresponds to $z_{p_{\odot,3.6}} = 24.842$. To convert from these units to solar masses per square parsec, two steps are used. The first is to derive the K -band M/L ratio from the corrected broadband colors. For $B - R$, the relation used is (Bell et al. 2003):

$$\log \frac{M}{L_K} = -0.264 + 0.138(\mu_B - \mu_R)_o$$

where $(\mu_B - \mu_R)_o$ is the Galactic reddening-corrected color index based on extinctions listed in NED. This relation differs substantially from that for the same color and near-IR band listed in Table 1 of Bell & de Jong (2001), which Bell et al. (2003) suggest is due to a larger metallicity scatter than accounted for in the earlier paper.

The second step is to convert $\frac{M}{L_K}$ into $\frac{M}{L_{3.6}}$. We used a simple relation due to Oh et al. (2008), based on stellar population synthesis models with a range of metallicities and star formation histories;

$$\frac{M}{L_{3.6}} = 0.92 \frac{M}{L_K} - 0.05$$

Because of the higher signal-to-noise in the $3.6\mu\text{m}$ image, it was not necessary to use the staggered median smoothing approach used for the SDSS images. The surface mass densities were then derived from the array values $C_{3.6}$ using

$$\Sigma(i, j) = C_{3.6}(i, j) \times 10^{-0.4(z_{p_{3.6}} - A_{3.6} - z_{p_{\odot,3.6}})} \times$$

$$0.92(10^{-0.264+0.138[\mu_B(i,j)-\mu_R(i,j)-A_B+A_R]}) - 0.05$$

For those cases where $B - V$ was used instead (NGC 628, 3351, 3627, and 5194), the M/L relation applied was (Bell et al. 2003)

$$\log \frac{M}{L_K} = -0.206 + 0.138(\mu_B - \mu_V)_o$$

where again the Galactic extinction corrections were taken from NED.

Addition of gas - Our analysis requires total mass maps, and thus it is essential to add in the contributions of atomic and molecular gas. Five of our sample galaxies were observed in The HI Nearby Galaxy Survey (THINGS; Walter et al. 2008), while M100 was observed as part of the VLA Imaging of Virgo Spirals in Atomic Gas (VIVA) program (Chung et al. 2009). All 6 are included in the BIMA Survey of Nearby Galaxies (BIMA SONG, Helfer et al. 2003). VIVA provides an HI image with resolution $31'' \times 28''$ and pixels $10'' \times 10''$. THINGS provides HI maps with a resolution of $\approx 6''$ and pixels $1''.5$ in size. The maps in all cases are publicly available, and the procedure for adding both HI and CO into the mass maps was the same. For the HI map, the total flux in the image was integrated to a radius consistent with the HI size of the object using IRAF routine PHOT. The map was then scaled to the measured total flux S_{HI} given in Table 5 of Walter et al. (2008) and in Table 3 of Chung et al. (2009). With this scaling, each pixel in the image then has the same units, Jy km s^{-1} , and can be converted to mass using $M_{HI}(i, j) = 2.36 \times 10^5 D^2 S_{HI}(i, j)$, where D is the distance in Mpc. Dividing each value by the number of square parsecs in a pixel, this gives the distance-independent surface mass density of HI gas in units of $M_{\odot} \text{pc}^{-2}$.

For the CO map, Table 4 of Helfer et al. (2003) gives the global CO flux, S_{CO} , for each galaxy. The same procedure as for the HI map gives the scaling of each pixel, such that the mass in each pixel is $M_{H_2}(i, j) = 7845.0 D^2 S_{CO}(i, j)$, where a conversion factor of $X = 2 \times 10^{20}$ has been used (Helfer et al. 2003). The scale of the publicly available images is $1''.0$ per pixel.

The pixel sizes of the two gas maps were different from the pixel sizes of the $3.6\mu\text{m}$ and i -band images. IRAF routine IMLINTRAN was used to create scaled maps with the same pixel sizes, outputted to an appropriate center of the galaxy. Each paper gave the right ascension and declination of the pointing center, which was compared with the coordinates in the RC3 to judge where we should set the centers in our mass maps. Each scaled map had its own flux-scale factor to keep the to-

tal masses the same as published by Helfer et al. (2003), Walter et al. (2008), and Chung et al. (2009).

Gravitational Potentials - The potentials were calculated using the 2D Cartesian approach outlined by Binney & Tremaine (2008) as described in ZB07 (and similar to the approach used by Quillen et al. 1994). An important parameter needed in this calculation is the vertical scale height, assuming an exponential vertical density distribution. We used the approximate radial scalelengths listed in Table 1 and information from de Grijs (1998) to judge scale heights. Being bright galaxies, there are other sources of radial scale-length determinations for our sample. A literature search showed good agreement between our estimated values and other sources except for NGC 4736, whose complex structure causes a large spread in values, and for NGC 5194, which is complicated by its companion.

Uncertainties in mass map determinations and derived results - The uncertainties in our mass maps come from a variety of sources. In general, photometric calibration uncertainties are small, and less than 0.05 mag. The principal uncertainties come from the M/L calibrations, effects of dust, and from deprojection and orientation parameter uncertainties. According to Bell et al. (2003), typical uncertainties in a color-dependent M/L involving a near-IR band (such as M/L_K) is ± 0.1 dex for redder $B - V$ and $B - R$ colors, and ± 0.2 dex for bluer colors. We have shown that the Bell et al. (2003) $B - V/B - R$ calibrations with $3.6\mu\text{m}$ as the base stellar mass image give azimuthally-averaged radial surface mass density profiles very similar to those given by the the Bell et al. (2003) $g - i$ calibration with the i -band as the base stellar mass image. From comparisons between the two base images and using also the Bell & de Jong (2001) $B - V/B - R$ calibrations, we found that phase shift distributions are more robust to M/L uncertainties than are mass flow rates, although even the latter agree fairly well between the two base images.

On the issue of orientation parameters, we did not experiment with different values but simply point to section 5.2 of BZ09 where tests were made of the impact of such uncertainties, including problems of bulge deprojection. The CR radii we list in Table 2 are for the assumed orientation parameters in Table 1.

Uncertainties in the assumed vertical scale-heights were examined for M100. Reducing h_z from $12''.6$ in Table 1 to $3''.8$ had almost no effect on the phase shift distribution. In the outer disk near 7 kpc, the flow rate is increased by about 10% but at 1 kpc the difference is about 30%. Thus even a drastic difference in h_z has only a relatively small effect on our results.

The issue of dust enters in the uncertainties in two

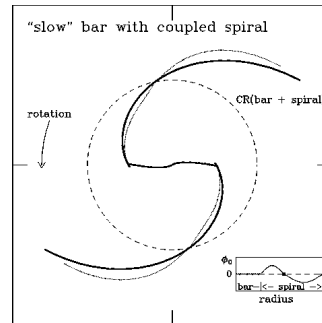


Figure 21: Schematic of the phase shift distribution for the slow bar.

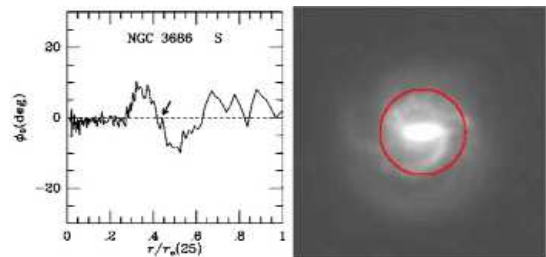


Figure 22: Examples of the phase shift distribution and morphology for the slow bar

ways: through the significant impact of dust on the optical M/L calibrating colors, and through the “hot dust correction” to the $3.6\mu\text{m}$ image. The former is less of a problem than might be thought. As noted by Bell et al. (2003), the effects of dust approximately cancel out to 0.1–0.2 dex when estimating color-derived M/L values because, in most passbands, stellar populations and dust predict about the same amounts of reddening per unit fading. That is, while dust reddens the starlight, redder colors imply higher M/L , which effectively can reduce the impact of dust lanes. Our results here basically verify this point. The uncertainty in the hot dust correction lies mainly in the factor $R_{3.6/8.0}$. We chose a low end value from Flagey et al. (2006) for this correction, but higher values may be appropriate for some galaxies (e.g., Kendall et al. 2008).

APPENDIX B. CATEGORIES OF BAR-SPIRAL MODAL MORPHOLOGY

In this appendix, we give schematics of the phase shift distributions of the various types of bar-spiral mor-

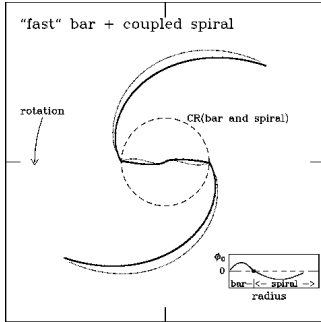


Figure 23: Schematic of the phase shift distribution for the fast bar with coupled spiral pattern.

phology, followed by examples of real galaxies that we have analyzed in BZ09. The sequence we present with these examples agrees roughly with the order of Hubble sequence from late to early, in order to show possible evolutionary connections between the various morphological patterns.

Figures 21 and 22 show a schematic and an example of a slow bar. This kind of bar is characterized by the fact that the bar ends well within its CR radius, with possible spiral structure emanating from the bar ends. The hosts are predominantly late-type galaxies, with a significant flocculent pattern in the outer regions. Closer inspection of the phase shift plot for NGC 3686 shows that around the location of the bar end, a new phase shift P/N transition is in the process of forming. Thus the slow bar appears to be a short-lived phase in the process of evolving into a bar-driven spiral, which we will analyze next.

Figures 23 and 24 show a schematic and an example of a fast bar with a coupled spiral, commonly referred to as a bar-driven spiral. This kind of pattern most often appears in intermediate-type galaxies, and appears to have evolved through stages of either a slow bar or else a skewed long bar.

Figures 25 and 26 show a schematic and two examples of fast bars with decoupled spirals. On one hand, these appear to be a further evolutionary stage of a bar-driven spiral, with the inner bar decoupled from the outer spirals and with the bar ends coinciding roughly with the CR radii. The signature of the decoupling (at the N/P phase shift crossing) shows up as branching of the spiral arms disconnected from the bar-end. Close inspection of the images and the phase shift plots show that the two examples we give will evolve into some-

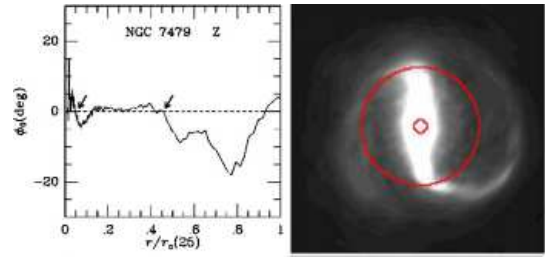


Figure 24: Examples of the phase shift distribution and morphology for the fast bar with coupled spiral pattern.

what different configurations later on: NGC 3507 appears to be evolving towards an inner bar-driven spiral followed by an outer spiral, whereas, NGC 150 appears to be evolving towards a super-fast bar with decoupled spiral that we will discuss next.

Figures 27 and 28 show a schematic and an example of a super-fast bar with a decoupled spiral. The phrase “super-fast” means that the bars extend significantly beyond their CR radii. In ZB07, we showed the case of a single isolated bar in the galaxy NGC 4665, where the bar extends about 10-20% beyond the PDPS-implied CR radius, and argued that in this case it is reasonable to expect the bar to be longer than the CR radius because the SWING amplified over-reflected waves from the inner disk must penetrate CR into the outer disk as a transmitted wave in order to have the overall angular momentum budget balance. In our current plot, the super-fast section of the bars are straight segments emanating from the location of an inner oval. The end of the bar coincides not with CR but with the next N/P phase shift crossing after the CR. This is reasonable because modal growth requires that for a complete self-sustained mode there must be a positive phase shift packet followed by a negative phase shift packet, with the two packets joining at CR – this in turn is because the density wave/mode has negative energy and angular momentum density inside CR (Shu 1992), and for its spontaneous growth the potential must lag the density – which leads to the positive potential-density phase shift – inside CR in order for the wave to torque the disk matter in the correct sense to lead to its own spontaneous growth by losing angular momentum to the disk matter. This is true vice versa for the modal content outside CR. Therefore, we see that for the kind of twin-bars joining the central oval the mode has little choice but to have the N/P phase shift crossing be at the end of the bar.

Direct evidence from morphology of NGC 4665 sup-

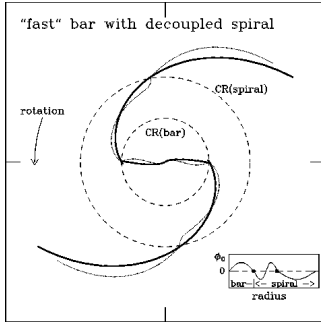


Figure 25: Schematic of the phase shift distribution for the fast bars with decoupled spiral pattern.

porting our claim that an N/P phase shift crossing for this galaxy coincides with the location where the modal pattern speed changes discontinuously is that there is a pronounced ring-like structure at the radius of the N/P crossing, obviously caused by the snow-plough effect of the interaction of the inner and outer modes. A similar configuration of a central oval joined by straight super-fast bars are also observed in NGC 3351, NGC 1073, NGC 5643, and in the central region of NGC 4321. As a matter of fact, since this configuration requires the central oval connecting to the straight bars, it is always found in the central configuration of nested modes.

Comparing the last two types of morphologies, we can clearly see that the “fast bars with decoupled spirals” appear to be evolving into “super-fast bars with decoupled spirals” I.e., in the phase shift plot for NGC 150 we see that a new P/N crossing at the end of inner oval is in the process of forming, or dropping down to zero. When it is fully formed this will become a super-fast bar.

It is no coincidence that the super-fast bars, which often appear in early type galaxies, have a more rounded nuclear pattern with two very straight segments connecting to it: both of these patterns correspond to very small phase shift. The largest phase shift occurs for patterns with 45° pitch angle, but when the pitch angle is close to 0° or 90° , the phase shift becomes zero. Small phase shifts lead to slow secular evolution rates as characterize early type galaxies. The fact that bar-driven spirals mostly have skewed nuclear bar patterns followed by trailing spiral segments that taper into narrow tails, whereas super-fast bars most often have rounded nuclear patterns followed by very straight bar segments which broaden into dumb-bell shaped pile-up of mate-

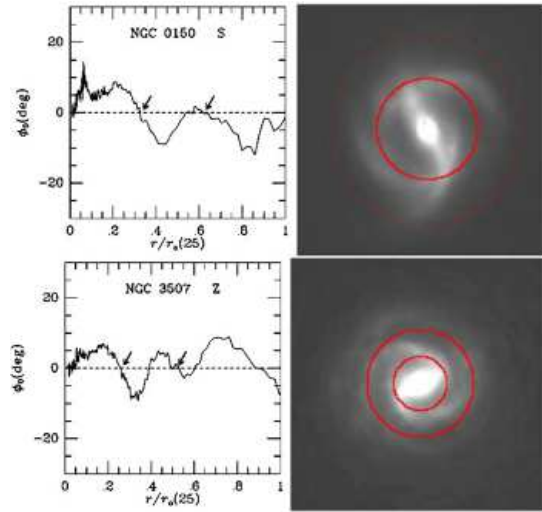


Figure 26: Examples of the phase shift distribution and morphology for the fast bars with decoupled spiral pattern.

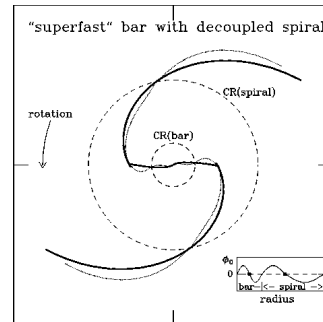


Figure 27: Schematic of the phase shift distribution for the super-fast bars with decoupled spiral pattern.

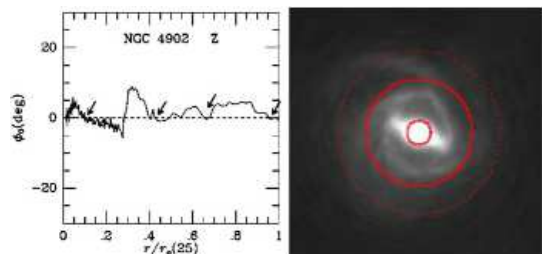


Figure 28: Examples of the phase shift distribution and morphology for the super-fast bars with decoupled spiral pattern.

rial at the mode-decoupling radii shows that super-fast bars are real, and are of completely different modal category than bar-driven spirals.

Note also that the above four categories are the main types of bar-spiral associations, and they do not exhaust all the morphological types encountered in real galaxies. For example, the above categories did not include the cases of either pure spiral galaxies (i.e. NGC 5247 analyzed in ZB07), or pure bar galaxies (i.e. NGC 4665 also analyzed in ZB07).

From the above analysis we see that distinctive phase shift patterns seem to delineate distinctive galaxy morphology proto-types, with the morphology of galaxies within a type category repeatable to a high degree. These morphological features also appear to correlate with the Hubble types of the basic state of the galactic disks (i.e., their being early, intermediate, or late). These correlations are naturally explained under the modal theory of density wave patterns (Bertin et al. 1989). The fact that the potential-density phase shift method can consistently classify the typical resonance structures for the given morphological types of galaxies shows that its success is not an accident, but rather supported by the underlying modal structure of the density wave patterns.